

## Magnetic phase-dependent Raman scattering in EuS and EuSe

R. P. Silberstein,\* V. J. Tekippe,\*† and M. S. Dresselhaus\*

*Department of Electrical Engineering and Computer Science and Center for Materials Science and Engineering,  
Massachusetts Institute of Technology, Cambridge, Massachusetts 02139*

(Received 9 May 1977)

Detailed evidence is presented linking the Raman spectra in the magnetic semiconductors EuSe and EuS to their respective magnetic phase diagrams. In particular, spectra for EuSe are presented for the paramagnetic, ferromagnetic, antiferromagnetic ( $\uparrow\downarrow\downarrow$ ), and ferrimagnetic ( $\uparrow\downarrow$ ) spin arrangements and are related to a Brillouin-zone-folding scheme for each magnetic sublattice structure. Based on our spectra, a set of phonon dispersion relations for EuSe in the  $\Gamma$ -L direction is constructed. We have also obtained for the first time right-angle Raman scattering spectra in EuSe. These results are compared with those obtained in the back-scattering geometry. Of significance is our observation that the broad spectral line extending from  $\omega_{TO}$  to  $\omega_{LO}$  in the paramagnetic phase persists for laser excitation energies below the fundamental absorption edge, thereby ruling out a hot luminescence mechanism for this feature. Instead our results are consistent with a spin-disorder model. Resonant Raman enhancement results are given for scattering in ferromagnetically ordered EuS and EuSe, and are related to magnetic-field-modulated magnetorefectivity spectra. Particular attention has been given to the magnetic-phase dependence of the EuSe modulated spectra in going from the ferrimagnetic to the ferromagnetic spin arrangements.

### I. INTRODUCTION

The europium chalcogenides (EuO, EuS, EuSe, and EuTe) were the first materials to be identified as magnetic semiconductors.<sup>1</sup> These compounds have attracted considerable interest in recent years because their magnetic structure has been found to influence their optical and transport properties significantly.<sup>1-3</sup>

The crystal structure in the paramagnetic state of the europium chalcogenides is isomorphic to that of NaCl and has fcc symmetry. First-order Raman scattering is therefore symmetry forbidden.<sup>4</sup> Nevertheless, first-order Raman scattering has been observed in all of these compounds. In particular we will present results for EuS and EuSe which show that the characteristics of the Raman spectra can be identified in detail with the magnetic-phase diagrams. The fact that each magnetic phase exhibits its own unique Raman spectrum implies that interactions with the spin system play an important role in the scattering mechanism. The observation of resonant scattering enhancement, particularly in the ferromagnetic phase, further implies that the scattering mechanism depends significantly on details of the electronic-energy-level scheme. Although studies of the energy-level scheme have previously been carried out using magnetorefectivity techniques, those studies were made in the Faraday geometry, whereas the present Raman measurements utilize the Voigt geometry. The necessity of correlating the resonance Raman results with the energy-level scheme therefore prompted the present study of magnetorefectivity in the Voigt geometry. Also

of interest are the correlations of the magnetorefectivity spectra with the details of the magnetic-phase diagram. Particular emphasis is given to EuSe in the low-magnetic-field regime where several distinct magnetic phases occur.

Section II reviews some of the basic properties of EuS and EuSe necessary for the understanding of the Raman scattering results. First, the magnetic properties of EuS and EuSe are summarized, emphasizing the details of the spin structure of each compound. This is followed by an overview of the electronic and optical properties and a survey of previous magnetorefectivity studies. Special attention is given to the status of Raman scattering research on these materials.

Section III describes the experimental apparatus and techniques, starting with the Raman scattering and magnetic-field-modulated reflectivity systems. Since the relation of experimental results to the magnetic-phase diagram is so important, demagnetization and thermal effects are then discussed since they relate to the accurate characterization of the scattering volume. The physical properties of the crystal samples used in the present work are then described. The discussion of experimental results in Sec. IV proceeds from Raman scattering spectra in the ferromagnetic phase, in the other magnetically ordered phases and, finally, in the paramagnetic phase. In particular, results for right-angle scattering are presented for laser excitation energies below the absorption edge. The magnetorefectivity spectra for EuSe are then described and related to the magnetic-phase diagram, leading to a discussion of resonant effects in the Raman scattering from the various magnetic phases.

Finally, Secs. V and VI discuss the experimental Raman results with particular reference to the magnetic-phase diagram. We propose a set of phonon dispersion relations to account for the phonons observed in the various magnetic phases of EuSe.

## II. BACKGROUND

### A. Magnetic properties

The dependence of the Raman scattering on the applied magnetic field, and in particular, on the detailed aspects of the magnetic-phase diagrams emphasizes the interconnection between the magnetic and electronic properties of these materials. These magnetic properties arise from the half-filled, localized  $4f$  shell of the europium ion and the superexchange interactions between neighboring magnetic ions.<sup>3,5</sup> A wide variety of magnetic phases is possible in the europium chalcogenide family because the nearest-neighbor and next-nearest-neighbor exchange constants,  $J_1$  and  $J_2$ , respectively, have similar magnitudes, but are opposite in sign. These exchange constants also depend differently on the distance between magnetic ions,<sup>3,6</sup> so that the magnetic order of each compound depends on the lattice constant  $a_0$ .<sup>7</sup> Of all the europium chalcogenides, EuS and EuSe have the most similar lattice constants, but their magnetic-phase diagrams are nevertheless very different due to small differences in their respective  $J_1$  and  $J_2$  values.

In EuS, the nearest-neighbor ferromagnetic interaction  $J_1$  dominates, and this material behaves as a simple ferromagnet with a Curie temperature ( $T_C$ ) of 16.5 K. EuS is an excellent example of a classical Heisenberg ferromagnet, and early studies<sup>8</sup> have shown that the temperature dependence of the magnetization in an applied magnetic field is well explained by a simple Weiss molecular field model. This simplicity stands in contrast to the behavior of EuSe.

In EuSe a variety of distinct magnetic phases is exhibited within a very small range of temperatures and magnetic fields, as shown by the phase diagram of Fig. 1.<sup>9</sup> Above the Néel temperature ( $T_N = 4.6$  K), EuSe is paramagnetic. In the absence of an applied magnetic field, EuSe is antiferromagnetic for  $2.8 < T < 4.6$  K and has a spin ordering labeled AF-I on the phase diagram. Within a given domain in the AF-I phase the spins are parallel to an equivalent  $[110]$  direction, and in successive  $(111)$  planes they are oriented  $\uparrow\uparrow\downarrow\downarrow$ .<sup>10</sup> This spin structure is illustrated in Fig. 2, which shows schematically the spins of the europium ions for the various low-temperature magnetic phases.

A small magnetic field applied to the AF-I phase

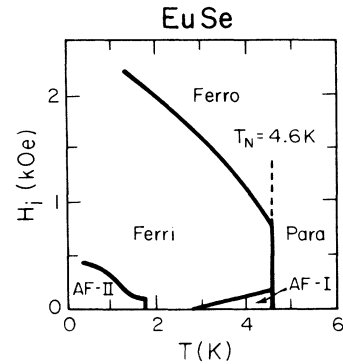


FIG. 1. Magnetic phase diagram of EuSe (Ref. 9).

can induce a transition to a ferrimagnetic phase (see Fig. 1). For this ferrimagnetic type of ordering, the spins in successive  $(111)$  planes are oriented  $\uparrow\uparrow\downarrow$ .<sup>10</sup> At lower temperatures,  $T < 1.8$  K, and for the internal magnetic field  $H_i \approx 0.40$  kOe (see Fig. 1), another antiferromagnetic phase, the AF-II phase, occurs in which the spins in alter-

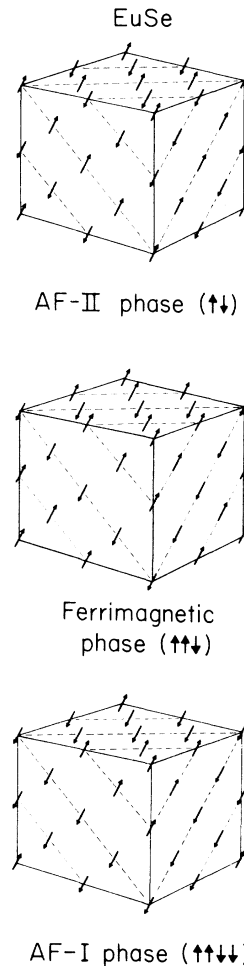


FIG. 2. Spin structure of EuSe for zero applied magnetic field in the AF-II, ferrimagnetic, and AF-I magnetic phases (see text). In the ferromagnetic phase and in the ferrimagnetic phase for  $H_i \geq 100$  Oe, the spins are parallel to  $\vec{H}$  (Ref. 12).

nate (111) planes are oriented  $\uparrow\uparrow\uparrow$ .<sup>9</sup>

The magnetocrystalline anisotropy of EuS and EuSe is small.<sup>11</sup> For  $H=0$  and  $T < T_C$  the preferred directions for spin alignment in EuS are the equivalent [111] directions,<sup>11</sup> but a domain aligning field of about 2 kOe at  $T \sim 2$  K is sufficient to align the spins parallel to the applied magnetic field. For  $H=0$  in EuSe and for all  $T < 4.6$  K, the spins within a given domain are parallel to an equivalent (111) plane, and lie along an equivalent  $[1\bar{1}0]$  direction.<sup>10</sup> In an applied magnetic field  $H_a$  such that  $H_i \gtrsim 100$  Oe, the spin direction is known to be parallel to  $H_i$ , independent of the orientation of  $H_i$  relative to the crystalline axes. This conclusion follows from measurements of the magnetization<sup>2, 12</sup> in the ferromagnetic phase ( $M_{\text{ferri}}$ ) and in the ferromagnetic phase ( $M_{\text{ferro}}$ ) which show that  $M_{\text{ferri}} \cong \frac{1}{2} M_{\text{ferro}}$ . In the ferromagnetically aligned spin phase, for  $H_a < M_s$  (saturation magnetization  $M_s$  in EuSe is 13.7 kOe),<sup>13</sup> a small anisotropy of about 15% of the saturation magnetization has been observed between the preferred directions ([111] and [110]) and the [100] direction.<sup>14</sup>

#### B. Electronic and optical properties

The electronic structure of the europium chalcogenides<sup>2,3</sup> is of importance to the Raman experiments because of the relation it bears to the resonant Raman process. The basic transitions are made from the localized  $4f^7 \ ^8S_{7/2}$  state of the europium ion to the  $t_{2g}$  sublevel of the  $4f^6 5d$  excited state which is split off from the higher-lying  $e_g$  level because of the cubic crystal field. The absorption edge or energy gap ( $E_g$ ) of the europium chalcogenides corresponds to the transition from the  $4f^7 \ ^8S_{7/2}$  state to the lowest level of the  $4f^6 5d t_{2g}$  multiplet which has been described according to various coupling schemes.<sup>2</sup>

In the europium chalcogenides the optical properties depend both on magnetic phase and temperature. The absorption edge, for example (see Table I), is at 1.65 eV for EuS at room temperature, is blue-shifted to  $\sim 1.69$  eV on cooling to 36 K,<sup>2</sup> and is red-shifted to 1.51 eV when the sample becomes ferromagnetically ordered for  $T < 4$  K.<sup>2</sup> This blue shift is also apparent in EuSe where, for  $H=0$ ,  $E_g$  shifts from 1.80 eV at room temperature to  $\sim 1.96$  eV at 2 K.<sup>15</sup> When the sample is ferromagnetically aligned by an external magnetic field, a further red shift of  $\sim 0.07$  eV occurs for  $T \ll T_N$ .<sup>2</sup> The absorption edge for EuS is low enough for this material to be opaque in the visible. The room-temperature absorption edge for EuSe, however, is at 1.80 eV, so that insulating samples are found to be transparent in the far red. The maximum absorption coefficient in the visible,  $\alpha_{\text{max}}$ , is  $\sim 1.5 \times 10^5 \text{ cm}^{-1}$  and occurs near 2.35 eV for EuS and 2.6 eV for EuSe.<sup>2,16</sup> This peak

TABLE I. Electronic and lattice parameters for EuS and EuSe.

Property	EuS	EuSe
Absorption edge (300 K) <sup>a</sup>	1.65 eV	1.80 eV
$E_1'$ <sup>b</sup>	1.64 eV	1.90 eV
$E_1$ <sup>b</sup>	1.89 eV	2.09 eV
$E_1''$ <sup>b</sup>	2.14 eV	2.35 eV
$\omega_{\text{LO}}$ (300 K) <sup>c</sup>	266.5 $\text{cm}^{-1}$	182 $\text{cm}^{-1}$
$\omega_{\text{LO}}$ (2 K) <sup>d</sup>	278 $\text{cm}^{-1}$	189 $\text{cm}^{-1}$
$\omega_{\text{TO}}$ (300 K) <sup>c</sup>	178.4 $\text{cm}^{-1}$	127.8 $\text{cm}^{-1}$
$\omega_{\text{TO}}$ (2 K) <sup>d</sup>	186.5 $\text{cm}^{-1}$	134.0 $\text{cm}^{-1}$
$a_0$ (4.2 K) <sup>e</sup>	5.951 Å	6.176 Å

<sup>a</sup>Reference 3.

<sup>d</sup>Reference 44.

<sup>b</sup>Reference 18.

<sup>e</sup>Reference 7.

<sup>c</sup>Reference 43.

in  $\alpha$  shows structure at low temperature which is sensitive to magnetic ordering.<sup>2,17</sup> Such magneto-optical effects are conveniently studied with the magnetorefectivity technique.

The magnetorefectivity spectra of EuS and EuSe have been measured previously,<sup>18</sup> but only in the ferromagnetic phase and in the Faraday geometry. Under these conditions the single broad peak observed in the unpolarized spectrum for  $H=0$  was found to split into three distinct components (referred to as  $E_1'$ ,  $E_1$ , and  $E_1''$ ) when a field of  $H=40$  kOe was applied to establish ferromagnetic spin ordering. The reflectivity peaks  $E_1'$ ,  $E_1$ , and  $E_1''$  are tabulated in Table I and are important for our understanding of the resonant Raman scattering data to be discussed in a later section of this paper. Greater sensitivity in studying the magneto-optical structure is obtained using polarization-modulation<sup>19</sup> and magnetic-field-modulation<sup>20</sup> techniques. This greater sensitivity of the modulation techniques is exploited when relating the magnetorefectivity spectra to the details of the magnetic-phase diagram (as is of interest in the case of EuSe), and when studying the effects of domain alignment on the reflectivity. Analysis of the modulated reflectivity spectra yields information on the coupling between the spin system and the electronic states<sup>21,22</sup> in contrast to our Raman experiments, which are related to the coupling between the spin system and the phonons.

#### C. Raman scattering studies

Compared with the reflectivity, the Raman spectra are more sensitive to the detailed symmetries of the magnetic phases and to the electronic-energy-level scheme of the europium chalcogenides. The Raman scattering in the paramagnetic phase of these materials<sup>23</sup> was found to consist of (i) a broad spectral line (the para line) of half width

$\sim 35 \text{ cm}^{-1}$  extending approximately from the zone-center TO-phonon to the LO-phonon frequencies with  $\omega_0$  defining the maximum scattering intensity, and (ii) harmonics of the para line at multiples of the fundamental frequency  $\omega_0$ . In EuS,<sup>24</sup> studies of the temperature dependence of the spectra in the paramagnetic phase show that the intensity of this line is related to the spin-correlation function. In ferromagnetically ordered EuSe, a narrower, magnetic-field-dependent Raman line is observed<sup>25</sup> close to the zone-center LO-phonon frequency ( $\omega_{LO}$ ); this line has been referred to as the "ferro line."<sup>26</sup> This LO-phonon scattering has its own series of harmonics and has been shown to be strongly resonant<sup>25-27</sup> near the energies of the  $E_1$  and  $E_1'$  magnetoreflexivity peaks of EuSe. Similar LO-phonon scattering phenomena have also been found in ferromagnetically aligned EuS,<sup>28</sup> EuTe,<sup>26,29,30</sup> and EuO.<sup>31,32</sup> Of significance are the different temperature dependences of the Raman scattering observed in the ferromagnetic and paramagnetic phases; this effect has been studied in detail for the case of EuS.<sup>28</sup>

The Raman scattering associated with the para line about  $\omega_0$  has been attributed to a spin-disorder model.<sup>23,28,33</sup> In the paramagnetic phase, where  $T > T_C$ , the spins are randomly aligned. As a consequence, the phonon-plus-spin system lacks both translational and inversion symmetry. As a consequence of the absence of translational symmetry, the crystal wave vector  $\vec{k}$  is no longer a good quantum number and phonon modes from throughout the Brillouin zone can participate in the Raman scattering process. Thus, in the paramagnetic phase first-order Raman scattering from the coupled phonon-spin system is expected to exhibit a broad structure extending from  $\omega_{TO}$  to  $\omega_{LO}$ . The fact that the higher harmonics of the para line exhibit essentially the same characteristics as the fundamental and occur at multiples of  $\omega_0$  rather than of  $\omega_{LO}$  suggests that the harmonics are due to the same type of scattering mechanism as the fundamental. When the translational symmetry of the lattice is restored by magnetic order, the first-order Raman scattering process becomes restricted to the zone-center optical phonon frequencies, in agreement with observations. Grünberg *et al.*<sup>32,34</sup> have calculated the phonon dispersion relations for the europium chalcogenides and have shown the density of phonon states to be especially large near the  $L$  point. They have also attributed the para line to a spin-disorder scattering mechanism, and on the basis of their phonon dispersion relations have identified the peak scattering intensity with contributions from  $L$ -point phonons. The literature is however unclear with regard to the scattering mechanism in the paramagnetic state.

A comparison between the Raman spectra in the europium and ytterbium chalcogenides has led Vintins and Wachter<sup>35-38</sup> to suggest hot luminescence as the scattering mechanism in the paramagnetic phase of the europium chalcogenides in contrast with the spin-disorder mechanism.<sup>23,27,28,33</sup>

In the low-field phases of EuSe where the magnetic unit cell differs from the chemical unit cell a folding of the Brillouin zone can occur and electron-phonon coupling to additional phonon modes can take place. The various Raman lines which have been observed in EuSe in the AF-I and ferromagnetic phases (the AF-I and ferro lines) have been attributed to these changes in the magnetic unit cell and the resulting zone-folding effects.<sup>26</sup> Characteristic spectra have also been observed<sup>31,39</sup> in antiferromagnetic EuTe which has the AF-II spin ordering. Some detailed work has also been carried out on the mechanism and selection rules for magnetic-phase-dependent Raman scattering.<sup>40-42</sup>

Infrared spectroscopic techniques such as reflectivity from single crystals<sup>43</sup> at 300 K and absorption by thin films<sup>44</sup> at 2 K have also been used to study the lattice mode frequencies of the europium chalcogenides. The values for  $\omega_{LO}$  and  $\omega_{TO}$  thus obtained are summarized in Table I. At present no other direct experimental information on the phonon dispersion relations for the europium chalcogenides is available although neutron diffraction results for magnon scattering have recently been reported.<sup>45</sup> The present study shows, however, that phonon frequencies at the  $\Gamma$  and  $L$  points in the Brillouin zone can be determined for all the europium chalcogenides using Raman scattering techniques, and at other points as well for materials having magnetic phases with magnetic unit cells larger than the chemical unit cell.<sup>26,40,41</sup>

### III. EXPERIMENTAL CONSIDERATIONS

#### A. Raman scattering system

Since EuS and EuSe are opaque in the visible, most of the Raman scattering experiments reported here are carried out in the back-scattering geometry using the system illustrated in Fig. 3. The Voigt configuration is used, in which the applied magnetic field is perpendicular to the plane of incidence. Laser excitation energies from  $\sim 1.9$  to 2.7 eV are provided by the discrete emission lines of an argon-ion laser and by a continuously tunable dye laser pumped by it. Fluorescence from the dye laser is eliminated with a Jarrell-Ash minichromator or with a series of narrow-band interference filters. Low temperatures are provided by Super Vari-Temp dewars, and measured by carbon resistance thermometers. Magnetic

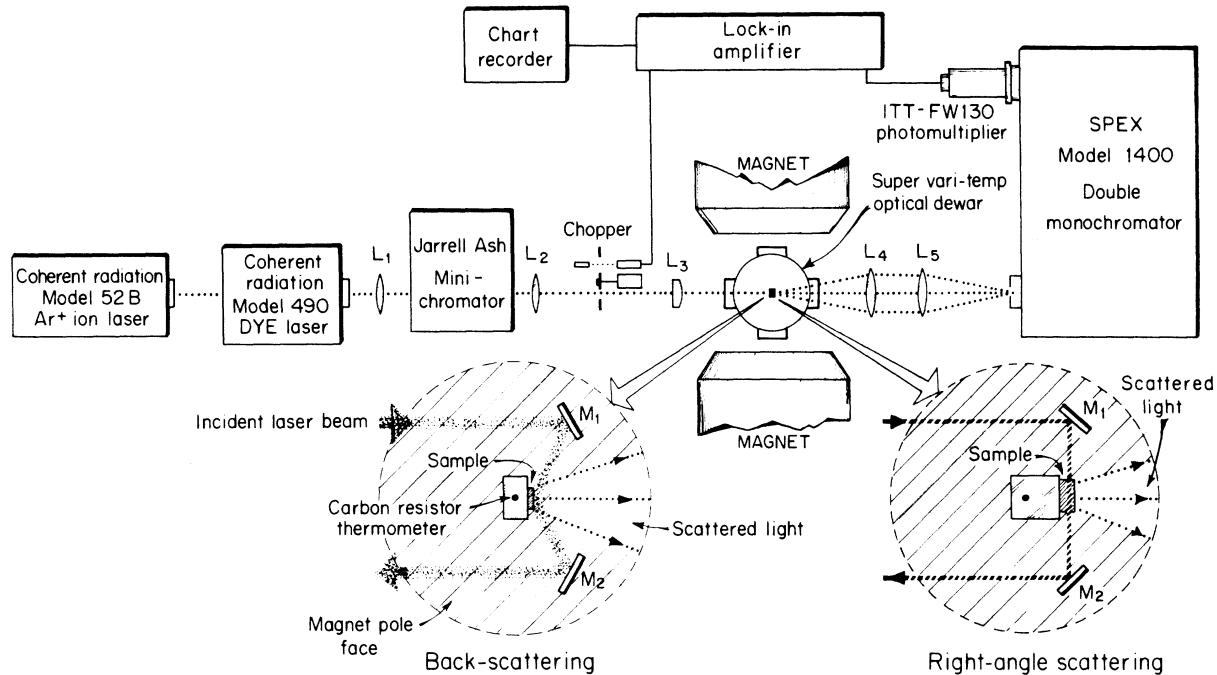


FIG. 3. Schematic diagram of the Raman scattering system. The insets show the geometries used for back-scattering (left) and right-angle scattering (right).

fields up to 10.5 kOe are obtained with a 12-in. Varian magnet, and fields up to 100 kOe with a radial-access Bitter solenoid (not shown). The scattered radiation is analyzed by a Spex model 1400 double monochromator and detected by a cooled ITT FW130 photomultiplier. Conventional phase-sensitive techniques are used for signal processing.

In the back-scattering geometry employed in the present study, the incident wave vector is usually inclined approximately  $45^\circ$  from the surface normal. At low temperatures the refractive index<sup>46</sup> of EuSe and EuS is approximately 2.6, so that within the crystal the incident wave vector is inclined about  $15^\circ$  from the normal. Experiments are also carried out with the incident wave vector within a few degrees of the surface normal.

For the study of right-angle Raman scattering in EuSe, laser excitation energies below the fundamental absorption edge are used. This configuration (See Fig. 3) has the advantage that the bulk of the crystal is probed rather than the skin depth, thereby increasing the light scattering volume and the Raman scattering intensity while reducing the effects of elastically scattered light from surface reflections and imperfections. The right-angle geometry has the further advantage that additional Raman selection rules can be studied in this configuration.

#### B. Magnetic-field-modulated magnetorefectivity

Since the present Raman experiments are carried out in the Voigt geometry, magnetorefectivity measurements are also made in the Voigt configuration in order to compare the selection rules governing reflectivity ( $R$ ) with those operative for the Raman process. Increased sensitivity is obtained by utilizing a magnetic-field-modulation technique in which a small ac component is added to the dc bias field. The ac modulation field allows phase-sensitive detection of the quantity  $(1/R)(dR/dH_a)\Delta H_a$  for each of the polarization directions used in the Raman measurements ( $\vec{E}_i \parallel \vec{H}_a$  and  $\vec{E}_i \perp \vec{H}_a$ ), where  $H_a$  refers here to the externally applied magnetic field. In addition, the dc bias field is varied so that different magnetic phases can be studied.

The apparatus used in the present study consists of a set of Helmholtz coils mounted on the sample holder itself and immersed in superfluid helium with the sample. The coils are driven by an audio oscillator and power amplifier and can develop modulation fields of over 120 Oe peak-to-peak (PP). Light from a monochromator passes through a polarizer and a chopper, is reflected from the sample at normal incidence, and is detected with a photomultiplier tube. One lock-in amplifier measures the component of the signal proportional

to  $(dR/dH_a)\Delta H_a$  and a second lock-in amplifier measures the component at the chopper frequency, proportional to  $R$ . The voltage on the photomultiplier is varied to keep  $R$  constant, so that  $(1/R) \times (dR/dH_a)\Delta H_a$  is normalized. The sensitivity of the apparatus for measurement of  $(1/R)(dR/dH_a)\Delta H_a$  is greater than  $5 \times 10^{-4}$ .

### C. Demagnetization corrections

The internal magnetic field  $H_i$  which is the field plotted on the magnetic-phase diagram differs from the applied magnetic field  $H_a$  according to the relation  $H_i = H_a - NM$ , where  $M$  is the magnetization of the sample and  $N$  is the demagnetizing factor for the particular sample geometry. To correlate Raman scattering or reflectivity results with the magnetic-phase diagram of EuSe, a demagnetization correction must be made in order to find  $H_i$ . The demagnetizing factor is difficult to derive in general, but complete tables are available<sup>47</sup> for the case of the general ellipsoid. From these tables an average volume demagnetization factor  $N_0$  can be derived for the samples. Since the region of interest is the reflecting or scattering volume within a skin depth from the surface, the average local demagnetization factor  $N_i$  is computed for the illuminated portion of the sample using a first-order theory for rectangular prisms.<sup>48</sup> For most cases  $N_i$  is close to and consistent with the estimate for  $N_0$ .

Having computed  $N_i$  for a particular sample shape and orientation, published magnetization data<sup>12</sup> for EuSe can be used to determine a calibration curve of  $H_i$  vs  $H_a$ . An example of such a calibration curve is given in Fig. 4 for one of the sam-

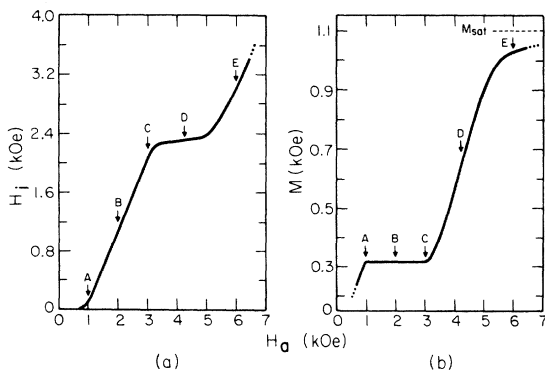


FIG. 4. Demagnetization corrections for an EuSe sample of dimensions  $2.4 \times 0.9 \times 0.3$  mm<sup>3</sup>, where  $\vec{H}_a$  is parallel to the 0.9-mm edge, the effective demagnetization factor  $N=2.89$ , and  $T \approx 2$  K (see text). (a)  $H_i$  vs  $H_a$ ; (b) magnetization ( $M$ ) vs  $H_a$ . Corresponding positions on the two curves are indicated: Points A, B, and C are for ferrimagnetic ordering; D denotes the ferri-to-ferromagnetic transition; E is typical of ferromagnetic spin alignment.

ples used in the present study. This sample is in the shape of a rectangular prism with  $N_i \sim 2.89$ . In Figs. 4(a) and 4(b), respectively,  $H_i$  and  $M$  are plotted as a function of  $H_a$ , with corresponding values of  $H_a$  on these curves labeled A, B, C, D, E to facilitate comparison of these curves. Knowing the range of  $N$  over the illuminated portion of the sample permits the calculation of the range of  $H_i$  corresponding to a given  $H_a$ . With this information it is thus possible to map out that part of the magnetic-phase diagram likely to be represented within the scattering volume in the Raman experiment.

### D. Thermal effects

Thermal homogeneity within the scattering volume is important. For example, in EuSe for  $H=0$ , different magnetic phases occur over a small temperature range (see Fig. 1). The sample is cooled to sample temperature  $T_s$  by mounting it on a copper cold finger which dips into the liquid helium. Sample temperatures above, but near, the boiling point of helium (4.2 K) are achieved by maintaining the level of the liquid helium a few centimeters below the level of the sample. For  $T_s=4.2$  K the level of the liquid helium I is maintained slightly above the lowest edge of the sample. For  $T_s$  below the  $\lambda$  point, the pressure is reduced and the entire sample and sample mount are immersed in superfluid helium. Over this temperature range,  $T_s$  is measured by a calibrated carbon resistor placed immediately behind the sample. This carbon resistance thermometer can only measure the average sample temperature, which, when in helium II, is practically identical to that of the helium bath. For the back-scattering geometry, however,  $T_s$  can vary significantly within the light scattering volume, which is defined by a strip approximately the length of the sample, but only  $\sim 50$   $\mu$  wide.

Studies of heat flow from solids immersed in superfluid helium<sup>49,50</sup> indicate that boundary effects can seriously impede the flow of heat across the solid-liquid interface, despite the extremely high thermal conductivity of helium II. Since most of the laser power is absorbed in a small region approximately  $0.3$   $\mu$  thick, this heat flux can raise the temperature of the scattering volume by as much as 2 K above that of the surrounding superfluid.<sup>50</sup> This temperature uncertainty is important in our experiments due to the sensitivity of the magnetic phase diagram to small changes in temperature. Such heating effects can be observed for laser powers as low as 20 mW and can actually be exploited in the back-scattering geometry for studying the ferrimagnetic and AF-I Raman spectra as a function of temperature. On the magnetic-phase diagram, this corresponds to moving

along the  $T$  axis for  $H = \text{constant}$  (see Fig. 1).

In contrast, measurements of the prominent LO-phonon line in ferromagnetically aligned EuS and EuSe are much less sensitive to laser heating provided that low power levels are maintained. For laser excitation energies below the absorption edge of EuSe, we use the right-angle scattering geometry. Because of the low optical absorption coefficient in this regime, laser heating effects are minimal and  $T_s$  is uniform throughout the scattering volume. It is of interest to note that as the liquid helium is brought in contact with the sample, the transition from the paramagnetic phase to the AF-I phase takes place and can be distinguished by a sudden onset of "milky" throughout the sample due to elastic scattering from microscopic antiferromagnetic domains.<sup>51</sup>

#### E. Samples

The single crystals of EuS and EuSe used in the present study were grown from europium-rich melts. Further annealing in an argon atmosphere improved the stoichiometry and produced samples which were highly insulating.<sup>52</sup> Although samples with different resistivities were tested, material with the highest resistivity consistently produced the strongest phonon Raman spectrum. Consequently all work reported here is for these insulating materials. We have also obtained single crystals grown from EuSe that was prepared by the reduction of  $\text{Eu}_2\text{O}_3$  by  $\text{H}_2\text{Se}$ .<sup>53</sup> These crystals are also highly insulating and their Raman spectra agree in detail with our samples grown from Eu-rich melts.

### IV. EXPERIMENTAL RESULTS

The Raman scattering spectra from EuS and EuSe can be correlated in detail with the features

of their respective magnetic phase diagrams. In particular, for EuSe the Raman scattering results are consistent with the *magnetic* unit cell rather than the *chemical* unit cell. The magnetic cell is defined by the spin arrangement in the ferromagnetic, AF-II, AF-I, ferrimagnetic, and paramagnetic phases (see Fig. 2). It is significant that the magnetic unit cell and hence the crystal symmetry is different for each of these magnetic phases.

#### A. Ferromagnetic phase

The simplest spin arrangement in EuS and EuSe occurs when all the spins are ferromagnetically aligned and the magnetic unit cell is the same as the chemical unit cell. In this case, first-order Raman scattering, when allowed, would be expected to occur from zone-center phonon modes. As will be discussed in a later section, resonant enhancement effects are important for the europium chalcogenides in making first-order Raman scattering detectable in the ferromagnetic state.<sup>30</sup> The relatively sharp ferro line (halfwidth of 8–11  $\text{cm}^{-1}$ ) and its harmonics characterize the Raman spectra in ferromagnetically aligned EuS and EuSe.<sup>25,28</sup> The ferro line appears within a few wave numbers of the zone-center LO-phonon frequency as deduced from low-temperature infrared absorption experiments on thin films.<sup>44</sup> Some of the principal characteristics of the ferro line and its harmonics in EuS are illustrated in Fig. 5 for  $H = 0$  and  $T = 2$  K.<sup>28</sup> The ferro line exhibits strong resonant enhancement near the  $E_1''$  peak in the magnetorefectivity spectrum (see Table I). For laser excitation energies near the  $E_1''$  peak, the ferro line is polarized  $\vec{E}_i, \vec{E}_s \perp \vec{H}_a$  when  $H_a$  is large enough to align the domains. At  $T = 8$  K the intensity of the ferro line is significantly reduced, and the broad para line begins to emerge. As  $T$  is in-

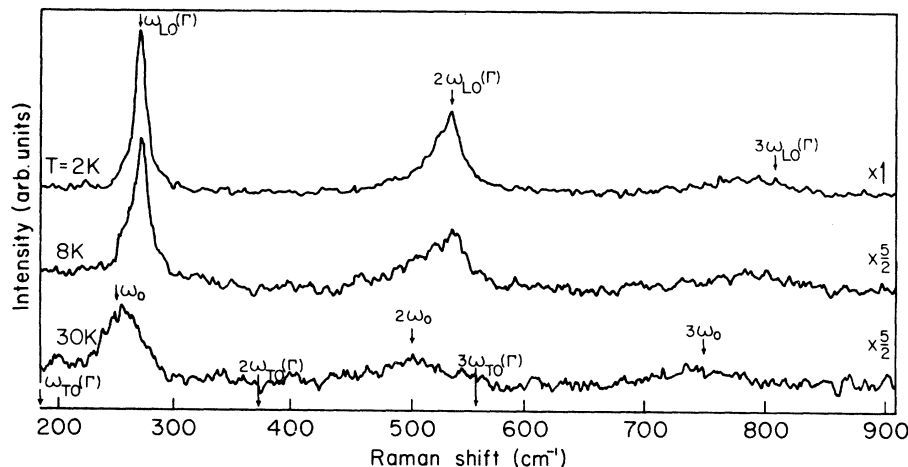


FIG. 5. Raman spectra of EuS for  $H_a = 0$  taken at  $T = 2, 8,$  and  $30$  K for  $E_L = 2.16$  eV ( $T_C = 16.5$  K). Multiples of  $\omega_0$ ,  $\omega_{LO}(\Gamma)$ , and  $\omega_{TO}(\Gamma)$  are indicated.

creased above  $T_c$ , the ferro line is quenched, so that the spectrum taken in the paramagnetic phase at  $T = 30$  K shows only the fundamental and harmonics of the para line. The fundamental ( $\omega_0 = 250$   $\text{cm}^{-1}$ ) has a linewidth of  $\sim 35$   $\text{cm}^{-1}$ , and for  $T = 300$  K and laser excitation energy  $E_L = 2.08$  eV, approximately 60% of the total scattered intensity is polarized  $\vec{E}_s \perp \vec{E}_i$ .

When a magnetic field is applied to EuSe for  $H_a \gtrsim 2$  kOe and  $T < 4.6$  K, the ferro line appears; this line is always polarized ( $\vec{E}_i, \vec{E}_s \perp \vec{H}_a$ ) and is quenched when an increase in temperature changes the spin ordering from ferromagnetic to paramagnetic (see Fig. 1). When the temperature is held constant near or below the transition temperature,<sup>27</sup> an increase in  $H_a$  enhances the intensity of the ferro line due to increased ferromagnetic ordering. Ultimately, the ferro line saturates when complete spin alignment is achieved.

As shown by the magnetic-phase diagram in Fig. 1, ferromagnetic spin ordering is not accessible in zero magnetic field in EuSe as it is in EuS, so that a direct comparison of the scattering intensity cannot be made for these materials at  $H = 0$ , but can be made at higher magnetic fields. Such a comparison is attractive due to the similar magneto-optical characteristics of these compounds when the spins are ferromagnetically aligned.<sup>2,3</sup> To relate the behavior of the ferro lines in EuS and EuSe, the temperature dependence of the peak scattering intensity is plotted in Fig. 6 for EuS at  $H = 0$ , and for EuSe at 5.0 and 10.5 kOe as a function of reduced temperature  $T/T_c$  where  $T_c$  is the critical temperature. For each curve, the peak intensity at  $\omega_{LO}$  is normalized to unity for  $T \gg T_c$ . Data were taken at incident laser energies where the ferro line is easily observed because of resonant enhancement effects. As shown in the figure, the ferro line is sharply enhanced in EuSe as  $T$  is reduced below  $T_c$  for  $H = 10.5$  kOe. We see that as the applied magnetic field is decreased from 10.5 to 5 kOe the temperature dependence of the scattering intensity curve for EuSe seems to approach that for ferromagnetically aligned EuS at  $H = 0$ . The self-consistency of this family of curves emphasizes the similarity of ferromagnetically ordered EuS and EuSe and suggests that the ferro line is common to all the ferromagnetically ordered europium chalcogenides. The ferro line has already been studied in some detail in ferromagnetically aligned EuTe for  $H > 70$  kOe<sup>26, 29, 30</sup> and these results together with preliminary results<sup>31, 32</sup> in EuO provide a consistent picture for Raman scattering in ferromagnetically ordered EuO, EuS, EuSe, and EuTe. With regard to the magnetic field dependence of the scattering intensity, the results for EuS and EuTe (Ref. 26)

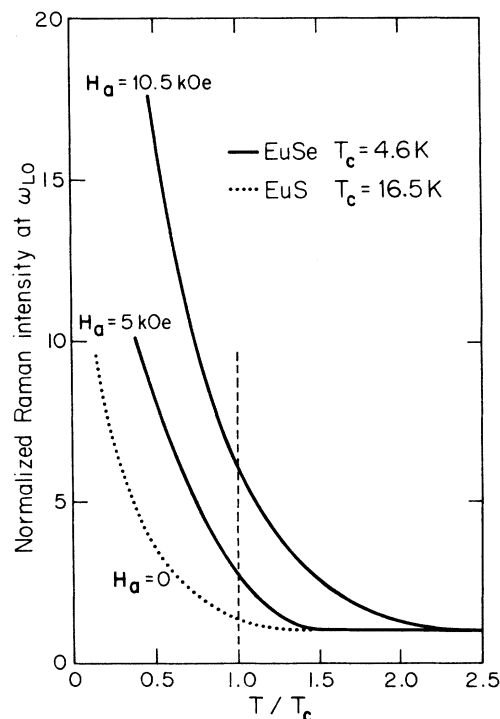


FIG. 6. Normalized peak Raman intensity of the ferro line at  $\omega_{LO}$  vs  $T/T_c$  for EuSe at  $H_a = 10.5$  and 5 kOe, and for EuS at  $H_a = 0$ . The scattering intensity at  $\omega_{LO}$  is normalized to 1 in the paramagnetic phase.

indicate that the intensity of the ferro line saturates when the applied magnetic field exceeds the critical field for ferromagnetic spin alignment by  $\sim 20\%$  to  $40\%$ . In EuSe we have found that when using a laser excitation energy of 2.41 eV the increase in the intensity of the ferro line for  $H_a \gtrsim 40$  kOe reported previously<sup>25</sup> was caused by laser heating (see Sec. III D).<sup>50</sup> This heating reduces the effective magnetization and decreases the spin alignment within the scattering volume, so that higher applied fields are required to observe magnetic saturation. This explanation of the previously reported high-field effect is verified by studying the magnetic field dependence of the intensity of the ferro line as the laser power is increased until the liquid helium boils at the sample surface. In Fig. 7 results are shown for the magnetic field dependence of the ferro line for a bath temperature of 1.3 K and  $E_L = 2.41$  eV; for these data the incident laser power is  $\sim 25$  mW. We denote this power level as *low* because at this level the saturation magnetic field does not shift with decreasing laser power. Using these low laser powers, the scattering intensity in EuSe saturates at 35 to 40 kOe (see Fig. 7). The saturation field observed in the present study agrees with that obtained by a study of Faraday rotation in EuSe at high magnetic fields.<sup>54</sup>

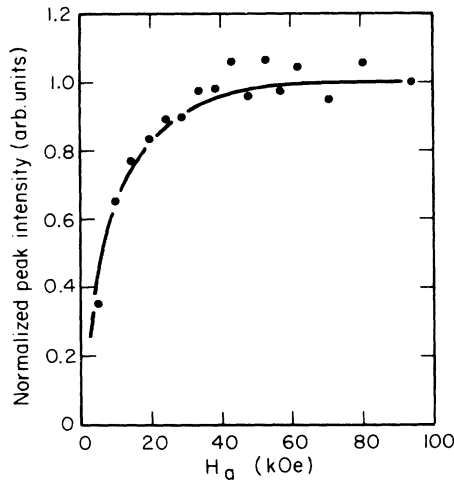


FIG. 7. Normalized peak intensity  $\omega_{LO}$  scattering intensity vs  $H_a$  for EuSe with  $E_L = 2.41$  eV ( $\lambda_L = 5145$  Å),  $\vec{E}_i \perp \vec{H}$ , and  $T$  (helium bath) = 1.3 K. A laser power of  $\sim 25$  mW was used. Each point represents an average of several measurements.

Also of interest is our observation of the ferro line for  $T > T_c$  (see Fig. 6), which we attribute to short-range order in the paramagnetic phase above but near  $T_c$ .

#### B. AF-II phase

The simplest type of magnetic ordering besides that in the ferromagnetic phase is the antiferromagnetic AF-II type of ordering observed in EuSe and EuTe. Here alternate (111) planes are oriented  $\uparrow\downarrow\uparrow\downarrow$  (see Fig. 2 which shows this phase for EuSe)<sup>10</sup>. The AF-II spin ordering in EuSe has been reported to exist in the ratio 5:13 with the ferrimagnetic spin ordering<sup>10</sup> at  $H = 0$  and  $T = 2$  K, but occurs only for  $T \lesssim 1.8$  K without admixture of other phases.<sup>9</sup> Consequently it is difficult to study the AF-II phase in EuSe by Raman spectroscopy in the back-scattering geometry because of laser heating effects. However, preliminary results<sup>26,31</sup> in EuTe show that a distinct Raman spectrum, suggestive of zone-edge phonons, is observed in this phase for  $T < T_N$ . It may be possible to minimize laser heating effects and study the AF-II phase of EuSe by using the right-angle configuration with laser excitation energies below the fundamental absorption edge.

#### C. AF-I and ferrimagnetic phases

Whereas the AF-II phase of EuSe is difficult to study with the Raman scattering technique, the AF-I and ferrimagnetic phases are readily accessible. Results for the Raman spectra in these phases have already been reported as a function of magnetic field using the back-scattering config-

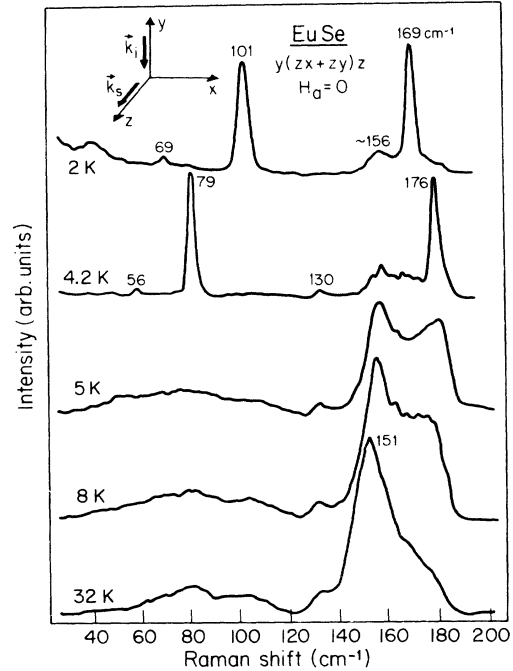


FIG. 8. Raman scattering spectra of EuSe in the right-angle configuration using the scattering geometry  $y(zx + zy)z$  (see inset), for  $H_a = 0$  and  $E_L = 1.91$  eV ( $\lambda_L = 6500$  Å). The curves are displaced vertically as appropriate for clarity, and the Raman frequencies for the principal spectral features are indicated for the paramagnetic phase (32 K, 8 K, 5 K), the AF-I phase (4.2 K), and the ferrimagnetic phase (2 K).

uration.<sup>26</sup> We present here the first observation of spectra in these phases using the right-angle geometry for which laser excitation energies below the fundamental absorption edge are employed. These results are of particular interest because of the observation of new effects in the right-angle geometry. An example of the results for this configuration is given in Fig. 8, which shows the Raman spectra of EuSe for several temperatures in the range  $2 \leq T \leq 32$  K for  $H = 0$  and  $E_L = 1.91$  eV ( $\lambda_L = 6500$  Å) which is below the fundamental absorption edge in this temperature range.<sup>15</sup> In the paramagnetic phase, the traces for  $T = 32, 8,$  and  $5$  K are seen to consist of several broad features which are discussed in Sec. IV D. As the temperature is lowered from 5 to 4.2 K corresponding to the paramagnetic to AF-I transition (see Fig. 1), the intensity of all the broad features is strongly quenched, and several sharp lines emerge. The AF-I lines at 79 and 176  $\text{cm}^{-1}$  have been discussed previously for the back-scattering geometry.<sup>26</sup> In addition, two weaker features can be distinguished in Fig. 8 at 56 and 130  $\text{cm}^{-1}$ , which we also associate with the AF-I phase because when  $T$  is reduced to 2 K the peaks at 56, 79, 130, and 176

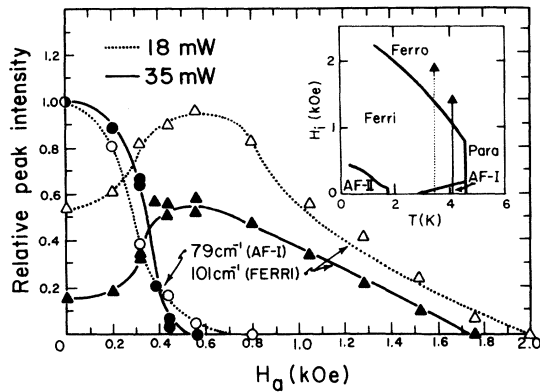


FIG. 9. Relative peak intensity of the Raman lines at 101 and 79  $\text{cm}^{-1}$  in EuSe vs  $H_a$  for laser powers of 18 mW (dotted curves) and 35 mW (solid curves). For these measurements  $E_L = 1.99$  eV ( $\lambda_L = 6250$  Å) and  $T$  (helium bath) = 2 K. The intensity of the line at 79  $\text{cm}^{-1}$  is normalized to 1 at  $H_a = 0$ . The inset shows schematically how the phases in the scattering volume change with  $H_a$ .

$\text{cm}^{-1}$  are all quenched. Note that the broad feature at  $\sim 156$   $\text{cm}^{-1}$  is associated with the para line and this line is quenched as  $T$  is reduced below  $T_N = 4.6$  K. At  $T = 2$  K, a feature at 69  $\text{cm}^{-1}$  is observed in addition to the lines at 101 and 169  $\text{cm}^{-1}$ , which we have previously identified with the ferrimagnetic phase.<sup>26</sup> Because of the similar temperature dependence of the 69-, 101-, and 169- $\text{cm}^{-1}$  lines, we also identify the 69- $\text{cm}^{-1}$  line with the ferrimagnetic phase.

An example of such an identification process is illustrated in Fig. 9 where the relative peak intensities of the 101- $\text{cm}^{-1}$  line and the 79- $\text{cm}^{-1}$  line are plotted as a function of  $H_a$  for two values of incident laser power ( $P_L$ ). For convenience, the intensity of the 79- $\text{cm}^{-1}$  line is normalized to 1 at  $H = 0$  for both laser powers, and the inset shows schematically how the phases within the scattering volume change with  $H_i$ . Using the inset to Fig. 9 and Fig. 4(a), we identify the 101- $\text{cm}^{-1}$  line with the ferrimagnetic phase and the 79- $\text{cm}^{-1}$  line with the AF-I phase because of their respective dependence on  $H_a$ . This identification is further confirmed by following the variation of the scattering intensity with temperature, where we assume that the temperature of the scattering volume is approximately proportional to the laser power. The association of each Raman line with a specific magnetic phase is consistent with the magnetic-phase diagram in detail (see Fig. 1) except for the behavior of the AF-I line in Fig. 9 at very low scattering intensities where intensity measurements are difficult to make. The magnetic field dependence of the lines at 176 and 169  $\text{cm}^{-1}$  is not shown in Fig. 9 because of the similarity of their

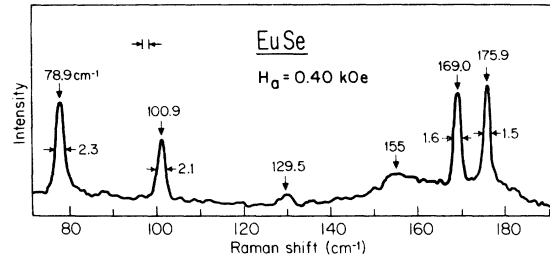


FIG. 10. Raman spectrum of EuSe in the back-scattering geometry for  $H_a = 0.40$  kOe,  $E_L = 1.99$  eV ( $\lambda_L = 6250$  Å) and  $T$  (helium bath) = 2 K. The lines at 79, 130, and 176  $\text{cm}^{-1}$  are AF-I lines while those at 101 and 169  $\text{cm}^{-1}$  are ferri lines. For  $H_a = 0.40$  kOe and a laser power of  $\sim 50$  mW, the scattering volume in the back-scattering geometry is a mixture of AF-I and ferri phases.

behavior with magnetic field and power level to the lines at 79 and 101  $\text{cm}^{-1}$ , respectively, thereby identifying the 176- $\text{cm}^{-1}$  line with the AF-I phase and the 169- $\text{cm}^{-1}$  line with the ferrimagnetic phase.

This identification of the Raman lines is used in the interpretation of spectra taken in the back-scattering configuration, as, for example, the spectrum shown in Fig. 10 for EuSe at  $H_a = 0.40$  kOe,  $E_L = 1.99$  eV ( $\lambda_L = 6250$  Å),  $P_L = 50$  mW and  $3 \lesssim T \lesssim 4$  K; this temperature variation over the scattering volume is caused by laser heating. The mean sample temperature can be varied by changing the power level, but this also changes the temperature spread. With the estimated temperature spread of  $3 \lesssim T \lesssim 4$  K,  $H_a = 0.40$  kOe results in a scattering volume in which both AF-I and ferrimagnetic ordering are present (see Fig. 1). Thus the spectrum in Fig. 10 shows ferri lines at 101 and 169  $\text{cm}^{-1}$ , AF-I lines at 79, 130, and 176  $\text{cm}^{-1}$  and a para line whose peak is at  $\sim 155$   $\text{cm}^{-1}$ .<sup>26</sup> These features are observed in both the diagonal ( $\vec{E}_i \parallel \vec{E}_s$ ) and off-diagonal ( $\vec{E}_i \perp \vec{E}_s$ ) polarization configurations.

The linewidths of the ferri and AF-I lines in the back-scattering geometry are considerably less (1.5 to 2.3  $\text{cm}^{-1}$ ) than those observed for the ferro line (8 and 11  $\text{cm}^{-1}$  for EuSe and EuS, respectively) or the paramagnetic line ( $\sim 30$   $\text{cm}^{-1}$ ). We note that the instrumental resolution for Fig. 10 is 1.5  $\text{cm}^{-1}$ . Due to the reduction in elastically scattered light for the right-angle geometry as compared with the back-scattering geometry, the weak lines at 56 and 69  $\text{cm}^{-1}$ , which we could not detect using back-scattering, are easily distinguished from the background with the right-angle geometry. The increased signal-to-noise ratio in the right-angle scattering geometry also permits the determination of the linewidths of the strong lines at 79, 101, 169, and 176  $\text{cm}^{-1}$  in this scattering geometry.

Based on additional spectra taken with high resolution (not shown), an upper limit to the linewidth is estimated to be  $0.6 \pm 0.1 \text{ cm}^{-1}$ . In the back-scattering geometry the lines at 79 and  $101 \text{ cm}^{-1}$  appear slightly broader than the lines at 169 and  $176 \text{ cm}^{-1}$ , whereas in the right-angle configuration the linewidths are the same to within  $\pm 0.1 \text{ cm}^{-1}$ .

For laser excitation energies below the absorption edge of EuSe, heating effects are reduced considerably. As shown in Fig. 8, there is negligible contribution from the AF-I lines to the spectrum at  $T = 2 \text{ K}$  and  $H = 0$ . This result is in agreement with the details of the magnetic-phase diagram in Fig. 1. It is significant that the right-angle scattering results give no evidence for a mixed magnetic state<sup>10</sup> at  $T = 2 \text{ K}$  and  $H_a = 0$ , which has been suggested to occur with an AF-II to ferrimagnetic ratio of 5:13.

Of significance to our interpretation of the Raman spectra in the ferrimagnetic and AF-I phases is the correspondence between the Raman lines observed in the back-scattering geometry above the absorption edge with the strong lines observed in the right-angle geometry below the absorption edge. The results obtained so far with both geometries support the identification of the ferri and AF-I lines with the occurrence of these phases on the magnetic-phase diagram.

#### D. Paramagnetic phase

The Raman scattering observed in the paramagnetic phase of all the europium chalcogenides consists of a broad line, the para line, extending from  $\sim \omega_{\text{TO}}$  to  $\sim \omega_{\text{LO}}$ . The association of this line with a first-order process in EuO,<sup>31</sup> EuS,<sup>23, 24</sup> EuSe,<sup>23</sup> and EuTe,<sup>26, 31</sup> is suggested by (i) the temperature dependence of this feature, (ii) the ratio of Stokes to anti-Stokes scattering, and (iii) the linewidths of the harmonics relative to the fundamental. The para line is strongly quenched when the spins become ferromagnetically aligned.

To distinguish between the spin-disorder and hot luminescence scattering mechanisms for the paramagnetic phase, we have carried out Raman scattering measurements on EuSe in the right-angle configuration for laser excitation energies  $E_L$  below the fundamental absorption edge, in a regime where the phonon-assisted luminescence process is prohibited by energy-conservation considerations. Our observation of a strong para line at  $\omega_0$  using laser excitation energies below the fundamental absorption edge, as well as the temperature dependence of the line shape both above and below the absorption edge are inconsistent with the hot luminescence mechanism for the europium chalcogenides. Furthermore, because of (i) the

strong quenching of the para line in the magnetically ordered phases and (ii) the temperature dependence of the para line shape, defect-induced Raman scattering can also be ruled out as the primary scattering mechanism for the para line.

However, these observations are consistent with spin-disorder scattering. By using laser excitation energies for which the ferro line is weak, it is possible to follow the para line well into the  $T \ll T_C$  regime. Such an experiment has in fact been carried out in EuS, where a residual scattering intensity was found at very low temperatures ( $T \ll T_C$ ). We attribute this residual scattering intensity to defect-induced scattering.<sup>28</sup>

Inspection of Fig. 8 reveals the characteristics of the spectra observed in the paramagnetic phase of EuSe with the right-angle scattering geometry. Of particular significance are the additional broad features which are observed with the right-angle geometry, but not with the back-scattering geometry. For example, the spectrum in Fig. 8 taken at  $T = 32 \text{ K}$  exhibits two broad overlapping peaks near 80 and  $100 \text{ cm}^{-1}$ . As  $T$  is decreased from 32 K, these broad structures decrease in intensity and at  $T = 5 \text{ K}$  can no longer be resolved. Additional measurements reveal, however, that on lowering the temperature to 5 K, the peaks close to 80 and  $100 \text{ cm}^{-1}$  remain and a new, weak feature at  $114 \text{ cm}^{-1}$  can be distinguished. These features are quenched when  $T$  is lowered below  $T_N$  and magnetic order is established. Because of the quenching phenomenon, we attribute the low-frequency broadline structures to spin-disorder scattering from acoustic phonons throughout the Brillouin zone. The width of the acoustic phonon branches is greater than that for optical branches, and hence a broader para Raman line is expected for the acoustic branches; this is consistent with our identification of the spectral features in Fig. 8. Our interpretation of the broad features in the 40– $120 \text{ cm}^{-1}$  range as arising from spin-disorder scattering from *acoustic* phonons (see Sec. V) also provides a consistent picture with our previously reported interpretation of the para line observed at higher frequencies in the back-scattering geometry as being associated with spin-disorder scattering from *optical* phonons.<sup>23, 27, 28, 33</sup>

The para line corresponding to optical phonons is also found in the right-angle geometry and appears as a broad, more intense structure with a peak intensity at  $\omega_0 = 151 \text{ cm}^{-1}$  for  $T = 32 \text{ K}$  (see Fig. 8). As the temperature is reduced to 8 K a feature emerges at  $\sim 176 \text{ cm}^{-1}$  within the linewidth of the broad structure. This structure becomes more pronounced as the temperature is lowered to 5 K. It is of interest that this feature has also been observed in the back-scattering geometry.

The intensity of the broad structure around the  $\omega_0$  peak generally decreases with decreasing temperature and the peak is up-shifted in frequency, shifting from  $151 \text{ cm}^{-1}$  at 32 K to  $156 \text{ cm}^{-1}$  at 5 K. As  $T$  drops below  $T_N$ , the broad band is quenched and the intense AF-I line at  $176 \text{ cm}^{-1}$  appears. These results are further discussed in Sec. V in connection with the phonon dispersion curves for EuSe.

A weak structure is also found near  $130 \text{ cm}^{-1}$ , appearing as a shoulder on the para line at 32 K, and as a resolved feature at lower temperatures for both right-angle and back-scattering geometries. Scattering near  $130 \text{ cm}^{-1}$  is also found at 4.2 K and associated with the AF-I phase (see Fig. 8). We note that in the AF-I phase this feature is sharper than the corresponding structure at  $130 \text{ cm}^{-1}$  in the paramagnetic phase. These relative linewidths are consistent with a para line centered at  $130 \text{ cm}^{-1}$  due to spin-disorder scattering from the entire TO phonon branch, and an AF-I line at  $130 \text{ cm}^{-1}$  arising from phonons in a localized region of the Brillouin zone, as will be discussed in Sec. V.

#### E. Magnetic-field-modulated reflectivity

To interpret the resonant-enhancement effects observed in the Raman scattering spectra (see Sec. IV F) and to correlate changes in the magnetorelectivity spectra with the magnetic phase diagram, magnetic-field-modulated reflectivity experiments were carried out using the Voigt geometry, the same configuration that was used for our Raman measurements.

It is significant that a large change in the intensity of the field-modulated spectrum is observed at a magnetic-phase transition such as the ferrito-ferromagnetic transition in EuSe. This effect is illustrated by the curves shown in Fig. 11. The inset of this figure shows the relative magnitude of the modulated reflectivity signal  $R_a \equiv (1/R)dR/dH_a$  observed at constant photon energy  $\hbar\omega = 2.39 \text{ eV}$  as a function of applied magnetic field  $H_a$  in the  $\vec{E}_i \perp \vec{H}_a$  geometry, as the field is swept continuously from  $H_a = 0$  to  $H_a = 8.0 \text{ kOe}$ . The photon energy of  $\hbar\omega = 2.39 \text{ eV}$ , near the  $E_1'$  magnetorelectivity peak shown in Fig. 12, is chosen because the energy of the  $E_1'$  peak does not change significantly for the magnetic field range of Fig. 11.

In this work the quantity of physical significance is  $H_i$  (the internal field, corrected for demagnetization effects) rather than the applied field  $H_a$ . Thus the data of the inset to Fig. 11 have been transformed from the  $H_a$  to  $H_i$  variable using the calibration curve of Fig. 4(a), and the results are then plotted in Fig. 11 in terms of  $R_i \equiv (dR/dH_i)/R$

$= (dH_a/dH_i)(dR/dH_a)/R$  vs  $H_i$ . Of significance is the lack of any strong variation in  $R_i$  with  $H_i$  except for the sharp peak at  $H_i = 2.3 \text{ kOe}$ , which is close to the ferrimagnetic-to-ferromagnetic transition as defined by the magnetization curve of Fig. 4(b). The sharp peak in  $R_i$  indicates a rapid increase in the reflectivity upon ferromagnetic spin alignment in agreement with the increase in  $R_i$  observed in EuTe when it becomes ferromagnetically aligned.<sup>19</sup> The decrease in  $R_i$  for  $H_i \gtrsim 2.5 \text{ kOe}$  indicates that the reflectivity saturates as the sample becomes fully magnetized. A similar behavior for  $R_i$  is observed at other photon energies.

Complementary to the results of Fig. 11 where the modulated reflectivity is plotted at constant  $\hbar\omega$  as a function of  $H_i$  are the results of Fig. 12 where  $R_a \Delta H_a$  for EuSe is plotted at constant  $H_a$  as a function of  $\hbar\omega$ . Reflectivity measurements in EuSe can be made over the range of photon energies shown on the abscissa of Fig. 12 because of the red-shift of the absorption edge at 2 K which occurs when a magnetic field aligns the spins ferrimagnetically<sup>55</sup> or ferromagnetically.<sup>2,55</sup> This red-shift extends the range of photon energies where EuSe is highly absorbing. The observed spectra of Fig. 12 depend on both the magnetic phase and on the polarization of incident light with respect to the applied magnetic field. For this reason data are presented at  $T = 2 \text{ K}$  for both the geometries  $\vec{E}_i \perp \vec{H}_a$  [Fig. 12(a)] and  $\vec{E}_i \parallel \vec{H}_a$  [Fig. 12(b)] for values of  $H_a = 1.06 \text{ kOe}$  (ferrimagnetic) and  $6.0 \text{ kOe}$  (ferromagnetic). In these measurements the modulation amplitude is  $\sim 120 \text{ Oe}$ . We note here that the Faraday geometry used for previous magnetorelectivity

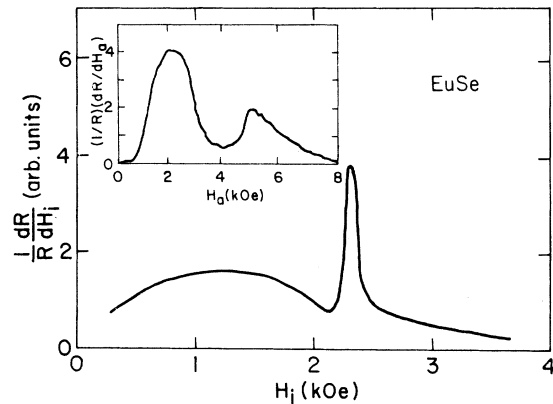


FIG. 11. Magnetic-field-modulated reflectivity amplitude for EuSe with  $\vec{E}_i \perp \vec{H}$ ,  $E_L = 2.39 \text{ eV}$ , and  $T = 2 \text{ K}$ . The magnitude of  $R_i = (1/R)(dR/dH_i)$  vs  $H_i$  is shown, where the peak in  $R_i$  at  $H_i = 2.3 \text{ kOe}$  is identified with the ferrito-ferromagnetic transition (see Fig. 1). The measured curve for  $R_a \equiv (1/R)(dR/dH_a)$  (arb. units) vs  $H_a$  is given in the inset, where the peak value of  $R_a$  at  $H_a = 2 \text{ kOe}$  is approximately  $0.036 \text{ kOe}^{-1}$ .

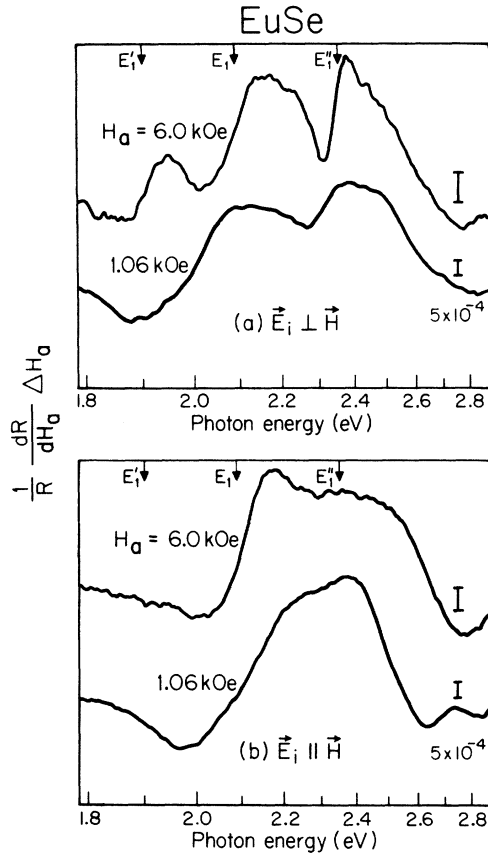


FIG. 12. Magnetic-field-modulated reflectivity spectra for EuSe in the Voigt geometry for (a)  $\vec{E}_i \perp \vec{H}$  and (b)  $\vec{E}_i \parallel \vec{H}$  at  $T = 2$  K, for applied fields of  $H_a = 1.06$  kOe (ferrimagnetic) and  $H_a = 6.0$  kOe (ferromagnetic). The vertical scale represents the quantity  $R_a \Delta H_a = (1/R)(dR/dH_a)\Delta H_a$ , where  $\Delta H_a$ , the modulation amplitude, is 120 Oe, and the error bar associated with each trace indicates the scale. Arrows indicate the positions of the  $E_1'$ ,  $E_1$ , and  $E_1''$  peaks from measurements in the Faraday geometry (Ref. 18).

studies<sup>18</sup> does not permit observation of a magnetorefectivity spectrum for the  $\vec{E}_i \parallel \vec{H}_a$  geometry.

In the case of ferromagnetic ordering (e.g.,  $H_a = 6$  kOe) three peaks are observed in the spectrum for the configuration  $\vec{E}_i \perp \vec{H}_a$ . These features coincide approximately with the  $E_1'$ ,  $E_1$ , and  $E_1''$  magnetorefectivity peaks which are observed with unpolarized light in the Faraday configuration<sup>18</sup> ( $H_a = 40$  kOe); the positions of these peaks are indicated in Figs. 12(a) and 12(b) by arrows. Table II summarizes the peak positions for the  $\vec{E}_i \perp \vec{H}_a$  geometry as shown in Fig. 12(a) and as determined previously.<sup>18</sup> For the  $\vec{E}_i \parallel \vec{H}_a$  geometry, however, an apparently unresolved doublet appears near the positions of the  $E_1$  and  $E_1''$  transitions. Another difference exhibited by the  $\vec{E}_i \parallel \vec{H}_a$  spectrum in the case of ferromagnetic spin alignment is the absence of the

TABLE II. Photon energies for the  $E_1'$ ,  $E_1$ , and  $E_1''$  peaks in eV for EuSe.

	Voigt <sup>a</sup>	Faraday <sup>b</sup>	Raman <sup>c</sup>
$E_1''$	2.37	2.35	2.39
$E_1$	2.16	2.09	~2.08
$E_1'$	1.95	1.90	

<sup>a</sup> Voigt refers to the magnetic-field-modulated reflectivity spectrum in the Voigt geometry at  $H_a = 6.0$  kOe (see Fig. 11).

<sup>b</sup> Faraday refers to reflectivity at high magnetic fields  $H_a = 40$  kOe in the Faraday geometry (Ref. 18).

<sup>c</sup> Raman refers to the resonant-enhancement curve for Raman scattering in the Voigt geometry (see Fig. 13).

peak near  $E_1'$ , which occurs in the  $\vec{E}_i \perp \vec{H}_a$  geometry at 1.95 eV.

By changing the bias field  $H_a$  to 1.06 kOe, the dependence of the magnetorefectivity spectra on the magnetic field configuration can be determined for the ferrimagnetic phase. Figure 12(a) shows the spectrum for  $\vec{E}_i \perp \vec{H}_a$  in the ferrimagnetic phase (1.06 kOe), and here only two peaks are observed at ~2.1 and 2.4 eV. In the ferrimagnetic phase, the linewidths are too large for the peaks to be fully resolved. Going from the ferrimagnetic to the ferromagnetic phase with  $\vec{E}_i \perp \vec{H}$ , the spectrum changes gradually to that shown in Fig. 12(a) for  $H_a = 6.0$  kOe where (i) the peaks are narrower and better resolved, (ii) a new low-energy peak appears at 1.95 eV, (iii) the central peak shifts upward to 2.16 eV, and (iv) the high-energy peak at 2.37 eV is at about the same energy as the peak occurring in the ferrimagnetic phase. For  $\vec{E}_i \parallel \vec{H}_a$  only a single broad peak centered near 2.3 eV is observed in ferrimagnetic EuSe, although the line-shape asymmetry suggests that it may be an unresolved doublet. While the center of gravity does not vary significantly with magnetic field for  $\vec{E}_i \parallel \vec{H}_a$ , small changes in the line shape can be observed as the applied magnetic field increases. The local maximum of the modulated reflectivity occurs near 2.38 eV for  $H_a = 1.06$  kOe, though for 6.0 kOe the peak occurs at 2.18 eV. An additional small peak is observed near 2.74 eV for  $H_a = 1.06$  kOe in the  $\vec{E}_i \parallel \vec{H}_a$  geometry. This structure in the magnetorefectivity of EuSe may be related to a feature reported in the magnetic-field-modulated reflectivity spectrum for EuS in the Faraday geometry<sup>20,31</sup> and to the structure observed on the high-energy side of the Faraday rotation spectra reported for EuS,<sup>56</sup> EuSe, and EuTe.<sup>54</sup>

The above discussion has shown that the magnetic-field-modulated reflectivity is magnetic-phase dependent and that the observed spectra in EuSe are consistent with the portions of the magnetic-phase diagram which are accessible with our ex-

perimental system. The magnetorefectivity results are thus in agreement with the present interpretation of the Raman scattering data. Further discussion of the magnetoreflexion spectra is given in the following section where a connection is made between the magnetorefectivity peaks and the energies where the resonant enhancement effects are most pronounced.

We have also carried out field-modulated magnetorefectivity measurements in EuS, where the only magnetically ordered phase is ferromagnetic. For each of the  $\vec{E}_i \perp \vec{H}_a$  and  $\vec{E}_i \parallel \vec{H}_a$  geometries, the spectra observed in EuS are similar to those observed in ferromagnetic EuSe. In the case of EuS, an overall enhancement of the magnetorefectivity structures is found when the magnetic field increases to line up the spins along the applied field.

#### F. Resonance effects

Since ordinary first-order Raman scattering from phonons is symmetry forbidden in the cubic europium chalcogenides, resonance effects are important in making the light scattering spectra observable in certain of the magnetic phases. The relation between the magnetic and chemical unit cells is magnetic-phase dependent. Since first-order Raman scattering involves only zone-center phonons, differences in the size of the magnetic unit cell results in differences in zone-folding. Consequently, phonons with different  $k$  vectors in the chemical Brillouin zone participate in the Raman scattering for the various magnetic phases. Because of this origin of the magnetic-phase-dependent Raman scattering, the resonance-enhancement effects are also magnetic-phase dependent. Since the optical transitions which give rise to the resonance Raman scattering are exhibited by peaks in the magnetorefectivity spectra, there is also a correlation between these two phenomena in the various magnetic phases.

The most striking resonance effects are observed in the case of ferromagnetic spin ordering. These resonance effects are illustrated in Fig. 13 where the laser-excitation-energy dependence of the scattering intensity is presented for ferromagnetically ordered samples of EuS, EuSe, and EuTe. In order to correct for the dependence of the scattering volume on laser excitation energy  $E_L$ , the quantity  $I/\delta$  is plotted vs the reduced laser energy parameter  $\epsilon \equiv (E_L - E_1'')/\hbar\omega_{LO}$  where  $I$  is the relative scattering intensity and  $\delta$  is the skin depth<sup>21,57</sup> at energy  $E_L$ . The points for different materials have been translated vertically on the logarithmic scale to account for the different skin depths, sample characteristics, and experimental systems used for each material. In this way, the

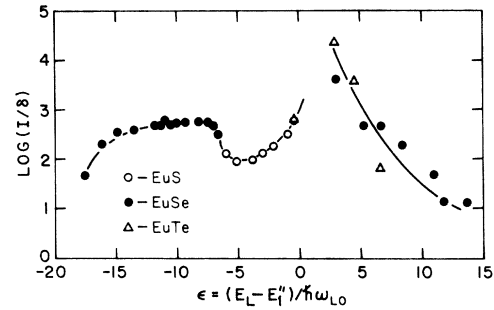


FIG. 13. Intensity of LO-phonon scattering in ferromagnetically ordered EuS, EuSe, and EuTe vs reduced laser excitation energy  $\epsilon = (E_L - E_1'')/\hbar\omega_{LO}$ . To present all the data on a single resonance curve, the logarithmic intensity scale is normalized for each compound separately. The intensity  $I$  is plotted in terms of the quantity  $\log(I/\delta)$  where  $\delta$  is the skin depth for each  $E_L$ . The data for EuS and EuSe are at  $H_a = 10.5$  kOe, and for EuTe at  $H_a = 95$  kOe; these field intensities are sufficient to produce ferromagnetic order in all three materials. The peaks correspond approximately to the  $E_1$  and  $E_1''$  magnetorefectivity peaks (Ref. 18).

data for all three compounds could be presented on a single curve. Of significance is the observation that the data points for all three ferromagnetically ordered materials fall on a *single* resonant curve.<sup>26,30</sup> In addition, two regions of resonant enhancement can be distinguished, corresponding approximately to the  $E_1$  and  $E_1''$  peaks in the magnetorefectivity spectrum,<sup>18</sup> and to the peaks in the modulated reflectivity spectrum as given in Table II. Of interest is the differing character of the two peaks in the Raman resonance curve, the low-energy peak being broad and weak, in comparison with the sharper and stronger peak near  $E_1''$ . Correspondingly, the field-modulated reflectivity peak near  $E_1''$  is sharper than the peak near  $E_1$  for the ferromagnetic phase (see Fig. 12). The shapes of the peaks near  $E_1''$  in both the Raman resonance and the field-modulated reflectivity spectra may be related to excitonic contributions from the  $4f^7 - 4f^6 5d t_{2g}$  transitions.<sup>40</sup> For ferromagnetic spin alignment, it is the zone-center LO phonon which contributes to the scattering process. Because of the equivalence of the magnetic and chemical unit cells in this case, resonance-enhancement effects are important in making the Raman scattering observable.

In contrast to the results for ferromagnetic spin ordering, the intensity of the para line is only weakly sensitive to  $E_L$  over the range of laser excitation energies shown in Fig. 12. This weak dependence on  $E_L$  is consistent with the broadness of the magnetorefectivity structure in this energy range in the paramagnetic phase. The absence of

a strong dependence on  $E_L$  of the scattering intensity does not rule out resonance effects playing a role in the scattering mechanism in the paramagnetic state. But since the contribution from zone-center ( $\Gamma$  point) phonons is very small in the para line, resonance-enhancement effects would not be expected to play an important role in the paramagnetic phase.

Resonance enhancement effects for the ferri and AF-I lines are also not as pronounced as for the ferro line and this is correlated with the relative broadness of the magnetoreflexivity structures in the ferrimagnetic and AF-I phases. Intensity variations of about a factor of 10 are observed for  $E_L$  in the range  $1.95 < E_L < 2.12$  eV, with the intensities of the AF-I lines being stronger than those for the ferri lines for larger values of  $E_L$ . It is of interest that the ferri and AF-I lines have been observed in the back-scattering geometry for  $E_L$  as high as 2.71 eV (which is nearly  $16\omega_{LO}$  away from  $E_1''$ ). The intensity variation of the ferri and AF-I lines with  $E_L$  may be due in part to  $E_L$ -dependent variations in laser heating. Such laser heating causes variations in the magnetic phase of the scattering volume, since the penetration depth changes rapidly over this range of  $E_L$ .<sup>21,50</sup> It is of interest to note that for the right-angle geometry and for laser excitation energies below the absorption edge, additional measurements show that the Raman scattering intensity in EuSe *per unit volume* is sharply reduced in comparison with the back-scattering geometry for all observed Raman lines, including the para, ferri, and AF-I lines.

Returning to the resonance-enhancement process for the ferro lines, the observed polarization selection rule of  $\vec{E}_i \parallel \vec{E}_s$  applies for all the europium chalcogenides in the vicinity of the  $E_1''$  peak. Although this selection rule is valid in EuSe for the entire range of laser excitation energies shown in Fig. 13, ferromagnetic EuS exhibits a variation of these polarization selection rules over a similar range of laser excitation energies. This is illustrated in Fig. 14 where we have plotted the magnetic field dependence of the polarization ratio  $p$  defined for the  $\vec{E}_i \perp \vec{H}_a$  geometry as

$$p \equiv \frac{I(\vec{E}_s \parallel \vec{E}_i)}{I(\vec{E}_s \parallel \vec{E}_i) + I(\vec{E}_s \perp \vec{E}_i)}$$

In this expression  $I$  is the intensity for a given polarization configuration, corrected for instrumental response.<sup>56</sup> It is significant that the data in Fig. 14 taken at the three laser excitation energies 2.140, 2.075, and 1.986 eV all give  $p=0.56$  for  $H_a \lesssim 1.5$  kOe. Since  $p=0.56$  corresponds to equal scattering intensity for  $\vec{E}_s \parallel \vec{E}_i$  and  $\vec{E}_s \perp \vec{E}_i$ , the observation of  $p=0.56$  for  $H_a \lesssim 1.5$  kOe is consistent with the presence of a set of microscopic, random-

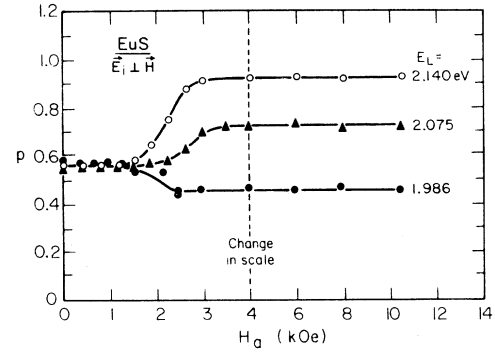


FIG. 14. Polarization ratio  $p$  vs  $H_a$  for EuS with  $\vec{E}_i \perp \vec{H}$  and  $T \approx 2$  K (see text for definition of  $p$ ). Curves are shown for  $E_L = 2.140$ , 2.075, and 1.986 eV. Note change in magnetic field scale at  $H_a = 4$  kOe. It is significant that  $p \approx 0.56$  for  $H_a \lesssim 2$  kOe and that  $p$  is a strong function of  $E_L$  when  $H_a \gtrsim 2$  kOe.

ly aligned ferromagnetic domains. A rapid change in  $p$  can be observed at  $H_a \approx 2$  kOe, corresponding to the alignment of ferromagnetic domains when the applied field exceeds the demagnetization field,  $NM_s$  (see Sec. III C).<sup>59</sup> For  $H_a \gtrsim 2.5$  kOe the polarization ratio saturates at a new value which is different for each laser wavelength. For example, for  $E_L = 2.14$  eV ( $\lambda_L = 5800$  Å), which is close to the  $E_1''$  magnetoreflexivity peak<sup>18</sup> and to the Raman scattering enhancement peak for EuS (see Fig. 13), the scattered radiation is polarized primarily  $\vec{E}_s \parallel \vec{E}_i$ . However, for  $E_L = 1.986$  eV ( $\lambda_L = 6248$  Å) which is closer to the  $E_1$  peak, the polarization of the ferro line is  $p = 0.47$ , which is essentially unpolarized.

These results, as well as those obtained at additional laser excitation energies but not shown in Fig. 14, are summarized in Fig. 15, where the polarization ratio  $p$  is plotted as a function of  $E_L$  for  $H_a = 0$  and  $H_a = 10.5$  kOe. For  $H_a = 0$ , Fig. 15 shows  $p$  to be independent of  $E_L$  with a value  $p \approx 0.56$  consistent with randomly aligned ferromagnetic domains. However, for  $H_a = 10.5$  kOe,  $p$  decreases monotonically from a value of 0.96 at  $E_L \approx E_1''$  to a value of  $\approx 0.5$  near the  $E_1$  structure. As mentioned previously, this behavior of the ferro line in EuS differs from that described earlier for EuSe, where the ferro line is only observed in the configuration  $\vec{E}_i \parallel \vec{E}_s, \vec{E}_i \perp \vec{H}_a$ , independent of  $E_L$ .

## V. DISCUSSION

In this section, the Raman results on the ferro line in EuS and EuSe are related to symmetry properties of the ferromagnetic phase. The right-angle scattering results for EuSe are then discussed with particular attention given to the para

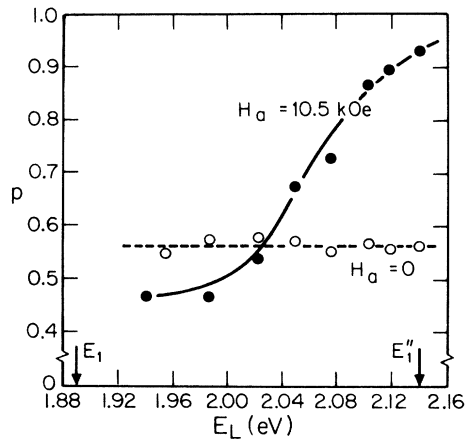


FIG. 15. Polarization ratio  $p$  (see text for definition) vs  $E_L$  for  $H_a = 0$  and  $H_a = 10.5$  kOe, where  $\vec{E}_i \perp \vec{H}$  and  $T = 2$  K. The  $E_1$  and  $E_1''$  positions from Faraday magnetoreflectivity measurements (Ref. 18) are shown by arrows. For  $H_a = 0$ ,  $p$  is constant, and  $\approx 0.5$ , whereas for  $H_a = 10.5$  kOe,  $p$  decreases markedly as  $E_L$  decreases from  $E_1''$  (maximum  $p$ ) to  $E_1$  (minimum  $p$ ).

line and to the identification of characteristic features in the various spectra with the appropriate magnetic phase and phonon mode. The different sizes of the magnetic unit cells for the various magnetic phases result in a magnetic-phase-dependent folding of the Brillouin zone. Consequently, first-order Raman scattering from each magnetic phase involves phonons with different  $\vec{k}$  vectors in the Brillouin zone for the chemical unit cell. Thus, from the Raman spectra for the various magnetic phases, phonon dispersion curves for EuSe along [111] can be determined and results from such an analysis are presented here.

In connection with the ferromagnetically ordered europium chalcogenides, a phenomenological scattering mechanism for the ferro line, which is observed close to  $\omega_{LO}$ , has recently been discussed.<sup>41</sup> It is found that when the normal electric-dipole-electric-dipole (ED-ED) Raman scattering is symmetry forbidden, as in the ferromagnetic phase of the europium chalcogenides, resonant Raman scattering arising from electric-dipole-electric-quadrupole (ED-EQ) or other wave-vector-dependent mechanisms<sup>60</sup> can nevertheless be observed. Further support for this interpretation of the ferro line comes from a theoretical study of the resonant enhancement process.<sup>40</sup> This study infers from the shape of the resonance curve near  $E_1''$  (see Fig. 13) that the peaks in the magnetoreflectivity spectra as well as in the resonant-enhancement curve for Raman scattering can result from interaction with a large number of magnetic excitonic levels. The validity of this interpretation will be further explored by resonant Raman

studies for  $E_L$  closer to the apparent peak of the resonant enhancement curve near  $E_1''$ . Presently, however, the range of energies near  $E_1''$  is difficult to obtain in EuSe and EuS using conventional laser and dye-laser systems.

The selection rules  $\vec{E}_i \parallel \vec{E}_s$ ,  $\vec{E}_i \perp \vec{H}_a$  observed for the ferro line in ferromagnetically ordered EuSe and EuTe are in good agreement with theoretical predictions,<sup>41</sup> which apply to the case where the spins are aligned parallel to  $\vec{H}_a$  and perpendicular to the phonon wave vector. Although these selection rules also apply to the ferro line in EuS for laser excitation energies  $E_L$  near  $E_1''$ , Figs. 14 and 15 show that these selection rules are relaxed as  $E_L$  approaches  $E_1$ , where the ferro line becomes observable in the  $\vec{E}_s \perp \vec{E}_i$ ,  $\vec{E}_i \perp \vec{H}_a$  configuration. Despite the discrepancy with the theoretical predictions, we believe this difference in selection rules to be a real experimental effect. In the back-scattering configuration a misalignment of the sample or of the demagnetization field could result in Faraday rotation of the incident and scattered light, but this effect is expected to be negligible due to the small skin depth,<sup>21</sup> despite the large magnitude of the Faraday effect in EuS.<sup>61</sup> Although magnetization-dependent birefringence in the Voigt geometry (the "Voigt effect") may produce effects as large as ordinary Faraday rotation,<sup>62</sup> the resulting depolarization of the Raman scattered light due to slight misalignments of  $\vec{E}_i$  is also expected to be negligible. An explanation for the anomalous polarization selection rule in EuS may ultimately depend on the contribution of higher-order processes or the participation of spin waves.

In the paramagnetic phase, the observation of the broad structure at  $\omega_0$  using laser excitation energies below the absorption edge of EuSe provides strong evidence that this structure is not due to a hot luminescence phenomenon. Support for the spin-disorder scattering mechanism comes from the close correlation of the observed spectral features with the magnetic-phase diagram. This interpretation is further supported by the change in line shape with temperature, as shown in Fig. 8. In cooling from 32 to 5 K, (i) the peak of the para line shifts by approximately  $5 \text{ cm}^{-1}$  to higher energies; (ii) the scattering intensity around  $140 \text{ cm}^{-1}$  decreases to the extent that the feature at  $130 \text{ cm}^{-1}$  is better resolved; and (iii) a second broad feature emerges near  $176 \text{ cm}^{-1}$ , as is also observed in the back-scattering geometry. This broad feature becomes an exceedingly narrow spectral line when  $T$  is reduced below  $T_N$  (as shown, for example, in the 4.2 K trace). These observations support the idea that in the paramagnetic phase the random spin alignment lifts the translational symmetry of the lattice, allowing

Raman scattering to take place by phonons throughout the Brillouin zone. Furthermore, as  $T \rightarrow T_N$  and the magnetically ordered phases are approached, long-range spin correlation begins to develop and broad structures arise in the vicinity of Raman frequencies corresponding to the appropriate magnetically ordered phases. The Raman contributions arising from this critical scattering process serve to alter the line shape of the parabolic line for  $T \geq T_N$  as compared with the line shape at high temperature  $T \gg T_N$ . For example, in Fig. 8, the broad shoulder at  $176 \text{ cm}^{-1}$  is identified with short-range order of the AF-I type and involving coupling to phonons near  $\frac{1}{2}k_{\text{max}}$  (where  $k_{\text{max}}$  corresponds to  $L$ -point phonons).<sup>63</sup> Finally, in the highly ordered AF-I phase at  $4.2 \text{ K}$  (see Fig. 8) the broad lines are quenched and only the sharp line at  $176 \text{ cm}^{-1}$  remains. Because of the quenching of the broad structure below  $120 \text{ cm}^{-1}$  as  $T$  falls below  $T_N$ , we attribute this low-frequency band to spin-disorder scattering from the acoustic modes. For the various magnetic phases of EuSe (see Figs. 1 and 2), the magnetic unit cell is elongated in the  $[111]$  direction according to the magnetic periodicity of the lattice.<sup>41</sup> This elongation of the magnetic unit cell results in a "folding" of the Brillouin zone along the  $[111]$  direction which permits electron-phonon coupling to zone-edge and mid-zone phonon modes. According to a detailed consideration of the spin symmetry and the magnetic Brillouin zone, it has been possible to select which phonon modes are expected to be Raman-allowed by the ED-ED mechanism.<sup>41</sup> In the two-sublattice AF-II phase, for example, only the zone-edge  $k_{\text{max}}$  LO( $L$ ) and TO( $L$ ) modes are expected to contribute to first-order Raman scattering, while for the three-sublattice ferrimagnetic phase, modes from all the branches at  $\frac{2}{3}k_{\text{max}}$  are allowed. For the four-sublattice AF-I phase the analysis predicts a coupling to the zone-edge  $k_{\text{max}}$  phonons on the acoustic branches and to the modes at  $\frac{1}{2}k_{\text{max}}$  for all the acoustic and optic branches.

With these selection rules as a guide, it is possible to construct the phonon dispersion relations of EuSe in the  $[111]$  direction using the observed Raman lines of Figs. 8 and 10. The result of such an analysis is shown in Fig. 16. In this set of dispersion relations,  $\omega_{\text{LO}}(\Gamma)$  is taken to be the frequency of the ferro line, while  $\omega_{\text{TO}}(\Gamma)$ , a mode which is symmetry-forbidden in the back-scattering geometry in the ferro phase of EuSe,<sup>41</sup> is taken from low-temperature ir absorption experiments<sup>44</sup> (see Table I). From the previous discussion of Figs. 8 and 10, the AF-I lines at  $176$ ,  $130$ ,  $79$ , and  $56 \text{ cm}^{-1}$  are assigned to the phonon modes at  $\frac{1}{2}k_{\text{max}}$  on the LO, TO, LA, and TA branches, respectively. Similarly, the ferri lines at  $169$ ,  $101$ , and  $69 \text{ cm}^{-1}$

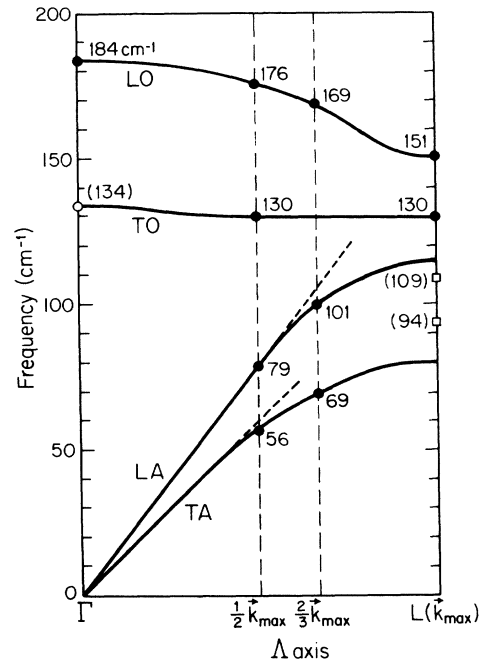


FIG. 16 Phonon dispersion relations for EuSe along the  $[111]$   $\Gamma$ - $L$  direction using our Raman-scattering results in the AF-I, ferri, ferro, and paramagnetic phases for both the back-scattering and the right-angle scattering geometries. The slopes of the dashed lines are obtained from the longitudinal and transverse  $[111]$  sound speeds calculated from the data of Ref. 65, the points marked  $\square$  are calculated from a one-dimensional model as described in the text and explicit values are given in parentheses; the point at  $\omega_{\text{TO}}(\Gamma)$  is taken from Ref. 44. The dashed lines denote  $\frac{1}{2}k_{\text{max}}$  and  $\frac{2}{3}k_{\text{max}}$ , where  $k_{\text{max}}$  is the wave vector at the  $[111]$  zone-edge  $L$  point. It is noteworthy that the spectral lines associated with longitudinal modes are strong, while those associated with transverse modes are weak.

$\text{cm}^{-1}$  are assigned to the phonon modes at  $\frac{2}{3}k_{\text{max}}$  on the LO, LA, and TA branches, respectively.

As yet, no light scattering features have been conclusively identified with the AF-II ( $\uparrow\uparrow\uparrow\uparrow$ ) antiferromagnetic phase of EuSe. Although it is possible in principle to carry out measurements for  $T \approx 1.8 \text{ K}$  in the right-angle geometry where laser heating is minimal, the apparent absence at  $T = 2 \text{ K}$  of features associated with the AF-II phase is noteworthy (see Sec. IV B).

Two major differences exist between the Raman selection rules<sup>41</sup> and the proposed dispersion diagram of Fig. 16: (i) the absence of LO( $L$ ) and TA( $L$ ) modes for the AF-II phase, and (ii) the absence of LA( $L$ ) and TA( $L$ ) modes for the AF-I phase. An interaction mechanism restricted to depend only on one power of the spin would indeed be consistent with the observation of modes at  $\frac{1}{2}k_{\text{max}}$  instead of at  $k_{\text{max}}$  for the AF-I phase.<sup>63</sup> Also

in agreement with this type of mechanism is the observation that in the back-scattering geometry the scattered light associated with phonons at  $\frac{1}{2}k_{\max}$  has a diagonal component ( $\vec{E}_i \parallel \vec{E}_s$ ) in addition to an off-diagonal one ( $\vec{E}_i \perp \vec{E}_s$ ).<sup>63</sup> Therefore we offer the dispersion relations in Fig. 16 as a revision of those which were tentatively proposed earlier<sup>41</sup> based on previously available experimental results. The present scheme differs from the earlier one in that for the revised version: (a) the AF-I lines are associated with phonon modes at  $\frac{1}{2}k_{\max}$  rather than at  $k_{\max}$ , (b) the peak of the paramagnetic line at  $\omega_0$  is identified with  $\omega_{LO}(L)$ , and (c) the TO and LA branches do not cross. It is interesting to note that the observation of both the diagonal and off-diagonal polarization components for the AF-I and ferri lines in the back-scattering geometry is consistent with the theory of Safran *et al.*,<sup>63</sup> but differs from that of Ousaka *et al.*,<sup>64</sup> who predict solely the antisymmetric component. Similar polarization results for the critical scattering structure near 176  $\text{cm}^{-1}$  for  $T \geq T_N$  also support the one-spin scattering mechanism.

In the paramagnetic phase, measurements of the peak position of the spin-disorder scattering ( $\omega_0$ ) in all the europium chalcogenides have been shown to be consistent with the identification of  $\omega_0$  as the frequency of the LO(L) phonon.<sup>32</sup> This identification follows from the especially high density of phonon states near the L point as reported by Grünberg *et al.*<sup>32</sup>; this identification is, however, independent of the applicability of their proposed excitation mechanism. A theoretical study of spin-disorder scattering by Safran *et al.*<sup>63</sup> also supports the identification of  $\omega_0$  with the LO(L) phonon. Contributions to the scattering intensity away from  $\omega_0$  come from phonons located elsewhere in the Brillouin zone, with very little intensity coming from frequencies  $\approx \omega_{LO}(\Gamma)$ .

In addition, Fig. 8 shows that for  $T > T_C$  there is a distinct local maximum at 130  $\text{cm}^{-1}$ , on the edge of the main structure, peaking at  $\omega_0$ . The Raman peak near 130  $\text{cm}^{-1}$  may arise from a high density of TO phonon states near 130  $\text{cm}^{-1}$  due to a relatively flat TO branch (see Fig. 16). In the paramagnetic phase, phonons from the entire TO branch can contribute to the spin-disorder scattering, but the largest density of states is near the L point and thus the peak of this Raman line is identified with  $\omega_{TO}(L)$ . Because the TO branch is flat,  $\omega_{TO}(\frac{1}{2}k_{\max}) \approx \omega_{TO}(L)$ , and the line observed in the AF-I phase is also near 130  $\text{cm}^{-1}$ . The line-width in this case is much smaller because only phonons in a small volume around  $\frac{1}{2}k_{\max}$  contribute to the scattering intensity in the AF-I phase. Using a one-dimensional model where  $\omega_{\text{acoustic}} = \omega_{\text{optical}}(M_{\text{Se}}/M_{\text{Eu}})^{1/2}$  at the L point, the points

marked by the open squares in Fig. 16 were calculated for  $\omega_{LA}(L)$  and  $\omega_{TA}(L)$  using the values assigned to  $\omega_{LO}(L)$  and  $\omega_{TO}(L)$ , respectively. Though meant only as zero-order approximations, these points are consistent with the Raman data in Fig. 16. The slopes of the dashed lines are the longitudinal and transverse sound speeds in the [111] direction,<sup>65</sup> and can be seen to agree well with the present assignments of the lines at 56 and 79  $\text{cm}^{-1}$ . Of further interest is the fact that every one of the Raman lines identified with *longitudinal* modes in Fig. 16 is very intense in comparison with every one of the observed lines identified with *transverse* modes. This difference in scattering cross section is consistent with the greater variation of the polarizabilities during a longitudinal vibration as compared with a transverse vibration. More detailed study of the Raman spectrum in the range 40–120  $\text{cm}^{-1}$  reveals a distinct shoulder at 114  $\text{cm}^{-1}$  for  $T=5$  K. We tentatively identify this weak feature with phonons near  $\omega_{LA}(L)$  in Fig. 16, although at the L point itself Raman scattering is symmetry-forbidden in the paramagnetic phase for both the TA and LA branches.<sup>63</sup> Finally, we have tentatively identified the two broad peaks at  $\sim 80$  and 100  $\text{cm}^{-1}$  observed at  $T=32$  K in Fig. 8 with spin-disorder scattering from the phonon modes near  $\omega_{TA}(L)$  and  $\omega_{LA}(L)$  where the density of states is large. However, contributions to the scattering intensities also arise from spin-disorder scattering by phonons associated with other points in the Brillouin zone in directions other than [111].

## VI. CONCLUDING REMARKS

To date, the different magnetic phases of the europium chalcogenide family have been studied by a number of investigators.<sup>24-33,36,38,66-70</sup> To unify these results, Table III lists references in the literature to studies of Raman scattering associated with the various magnetic phases of the europium chalcogenides. Common themes in many of these studies have been the relationship of the observed light scattering spectra to the electronic states, to the phonons, and to the details of the spin symmetry.

In this paper we have presented Raman scattering results for the magnetic semiconductors EuS and EuSe and have shown that the spectra are intimately correlated with the details of their respective magnetic-phase diagrams. We have studied the resonance-enhancement effects associated with the LO-phonon scattering in the ferromagnetic phase of the europium chalcogenides, and as part of this effort have carried out magnetic-field-modulated reflectivity experiments in the ferrimagnetic and ferromagnetic phases of EuSe. The results

TABLE III. References in the literature to studies of Raman scattering associated with magnetic phases of europium chalcogenides.

Phase \ Compound	EuO	EuS	EuSe	EuTe
		Reference numbers in text		
Ferro (++++)	31,32	24,26,28, 30,31,32, 33	25,26,27, 30,33,36, 38,67	26,29,30
AF-II (++++)			70	26,31,36
Ferri (+++)			26,68	
AF-I (++++)			26,68	
Para	23,31,32	23,24,28, 31,32,33, 36,38,66	23,27,32, 33,36, 38, <sup>a</sup> 67,68	23,26,29, 31,32,36, 69

<sup>a</sup>Measurements of the para line were also made at 1.8 K with  $H = 0$  and 10 kOe.

of these reflectivity studies indicate that important changes in the spectra occur as a function of magnetic phase. In EuS, interesting polarization effects are observed for the Raman ferro line as a function of laser excitation energy indicating that the present theoretical understanding of this phenomenon will have to be expanded. In EuSe, the study of right-angle scattering spectra has resulted in the discovery of several new features associated with the ferri- and AF-I phases. The observation of the broad line at  $\omega_0$  for laser excitation energies below the absorption edge of EuSe provides strong evidence against the hot luminescence model and favors the spin-disorder model for Raman scattering in the paramagnetic phase of the europium chalcogenides. Changes in the line shape of the broad line at  $\omega_0$  have been observed in the paramagnetic phase of EuSe as  $T \rightarrow T_N$  for both the back-scattering and the right-angle geometry. These changes in line shape are consistent with the critical scattering mechanism of Safran *et al.*<sup>63</sup> at  $\frac{1}{2}k_{\max}$ . The strong temperature dependence of structure within the line shape of the Raman line in the paramagnetic phase as  $T_N$  is approached indicates the importance of critical scattering from spin fluctuations. In addition, the results of the Raman study of spin-dependent phonon scattering have been used to map out part of the phonon dispersion relations of EuSe, and these results are in qualitative agree-

ment with recent phonon dispersion calculations.<sup>34,64</sup> We have thus shown evidence that the details of the spin symmetry are of great importance in accounting for the Raman scattering results in the various magnetic phases of EuSe and EuS. It is therefore expected that the application of symmetry analysis to the antiferromagnetic and canted-spin phases of EuTe will prove of similar usefulness.

*Note added in proof.* Recently we have observed Raman spectra which are associated with the AF-II phase of EuSe for  $T < 1.8$  K. We have also confirmed that the ferro line in EuSe can be observed with  $\vec{E}_i \perp \vec{E}_s$  for  $E_L$  far from  $E_1''$ , as reported here for EuS. These results will be described elsewhere.<sup>70</sup>

#### ACKNOWLEDGMENTS

We are grateful to Dr. T. B. Reed and R. H. Fehy for providing us with samples of EuS and EuSe, and to Professor G. E. Everett for additional samples of EuSe prepared by different methods. We also wish to thank S. A. Safran, L. E. Schmutz, Dr. G. Dresselhaus, and Dr. Y. Shapira for many useful discussions. Technical assistance from Dr. R. L. Aggarwal, L. Rubin, L. V. Sousa, and the staff of the Francis Bitter National Magnet Laboratory is greatly appreciated.

\*Visiting Scientist, Francis Bitter National Magnet Laboratory. Supported by the NSF, Grant No. 7302473-A01-DMR.

†Present address: Department of Physics, University of Illinois, Chicago Circle, Box 4348, Chicago, Ill. 60680.

<sup>1</sup>S. Methfessel and D. C. Mattis, in *Handbuch der Physik*, edited by S. Flugge (Springer-Verlag, Berlin, 1968), Vol. 18-1, p. 289.

<sup>2</sup>P. Wachter, *Crit. Rev. in Solid State Sci.* **3**, 189 (1972).

<sup>3</sup>G. Güntherodt, *Phys. Kondens. Mater.* **18**, 37 (1974).

<sup>4</sup>R. Loudon, *Adv. Phys.* **13**, 423 (1964).

<sup>5</sup>J. B. Goodenough, in *Magnetism and the Chemical Bond* (Wiley, New York, 1963), pp. 149, 167.

<sup>6</sup>T. R. McGuire and M. W. Shafer, *J. Appl. Phys.* **35**, 984 (1964).

<sup>7</sup>F. Lévy, *Phys. Kondens. Mater.* **10**, 71 (1969).

- <sup>9</sup>U. Enz, J. F. Fast, S. van Houten, and J. Smit, *Philips Res. Rep.* **17**, 451 (1962).
- <sup>9</sup>R. Griessen, M. Landolt, and H. R. Ott, *Solid State Commun.* **9**, 2219 (1971).
- <sup>10</sup>P. Fischer, W. Hälgl, W. von Wartberg, P. Schwob, and O. Vogt, *Phys. Kondens. Mater.* **9**, 249 (1969).
- <sup>11</sup>M. C. Franzblau, G. E. Everett, and A. W. Lawson, *Phys. Rev.* **164**, 716 (1967); R. F. Brown, A. W. Lawson, and G. E. Everett, *Phys. Rev.* **172**, 559 (1968).
- <sup>12</sup>C. Kunzia and G. Kneer, *Phys. Lett. A* **27**, 664 (1968).
- <sup>13</sup>U. Köbler and K. J. Fischer, *Z. Phys. B* **20**, 391 (1975).
- <sup>14</sup>P. Schwob and O. Vogt, *Phys. Lett.* **22**, 374 (1966).
- <sup>15</sup>P. Wachter, in *Handbook on the Physics and Chemistry of Rare Earths*, edited by K. A. Gschneidner, Jr. and L. Eyring (North-Holland, Amsterdam, to be published), Vol. 1, Chap. 19.
- <sup>16</sup>S. van Houten, *J. Phys. Chem. Solids* **17**, 7 (1960).
- <sup>17</sup>T. Mitani, M. Ishibashi and T. Koda, *J. Phys. Soc. Jpn.* **38**, 731 (1975).
- <sup>18</sup>C. R. Pidgeon, J. Feinleib, W. J. Scouler, J. Hanus, J. O. Dimmock, and T. B. Reed, *Solid State Commun.* **7**, 1323 (1969).
- <sup>19</sup>C. R. Pidgeon, J. Feinleib, and T. B. Reed, *Solid State Commun.* **8**, 1711 (1970).
- <sup>20</sup>G. Güntherodt and P. Wachter, *Surf. Sci.* **37**, 288 (1973).
- <sup>21</sup>J. Schoenes, *Z. Phys. B* **20**, 345 (1975).
- <sup>22</sup>T. Kasuya, *Crit. Rev. in Solid State Sci.* **3**, 131 (1972).
- <sup>23</sup>J. C. Tsang, M. S. Dresselhaus, R. L. Aggarwal, and T. B. Reed, *Phys. Rev. B* **9**, 984 (1974).
- <sup>24</sup>A. Schlegel and P. Wachter, *Solid State Commun.* **13**, 1865 (1973).
- <sup>25</sup>J. C. Tsang, M. S. Dresselhaus, R. L. Aggarwal, and T. B. Reed, *Phys. Rev. B* **9**, 997 (1974).
- <sup>26</sup>R. P. Silberstein, L. E. Schmutz, V. J. Tekippe, M. S. Dresselhaus, and R. L. Aggarwal, *Solid State Commun.* **18**, 1173 (1976).
- <sup>27</sup>V. J. Tekippe, R. P. Silberstein, M. S. Dresselhaus, and R. L. Aggarwal, *Proceedings of the Twelfth International Conference on the Physics of Semiconductors, Stuttgart, Germany, 1974*, edited by M. H. Pilkuhn (Teubner, Stuttgart, 1974), p. 904.
- <sup>28</sup>V. J. Tekippe, R. P. Silberstein, M. S. Dresselhaus, and R. L. Aggarwal, *Phys. Lett. A* **49**, 295 (1974).
- <sup>29</sup>L. E. Schmutz, V. J. Tekippe, R. L. Aggarwal, and M. S. Dresselhaus, *Bull. Am. Phys. Soc.* **20**, 379 (1975).
- <sup>30</sup>V. J. Tekippe, R. P. Silberstein, L. E. Schmutz, M. S. Dresselhaus, and R. L. Aggarwal, *Proceedings of the Third International Conference on Light Scattering in Solids, Campinas, Brazil, 1975*, edited by M. Balkanski, R. C. C. Leite, and S. P. S. Porto (Wiley, New York, 1976), p. 362.
- <sup>31</sup>G. Güntherodt, *Proceedings of the Thirteenth International Conference on the Physics of Semiconductors, Rome, 1976*, edited by F. G. Fumi (Tipografia Marves, Rome, 1976), p. 291.
- <sup>32</sup>P. Grünberg, G. Güntherodt, A. Frey, and W. Kress, *Physica B* **89**, 225 (1977).
- <sup>33</sup>V. J. Tekippe, R. P. Silberstein, M. S. Dresselhaus, and R. L. Aggarwal, *The Application of High Magnetic Fields in Semiconductor Physics: Lectures Presented at the International Conference, Würzburg, Germany, 1974*, p. 449.
- <sup>34</sup>P. Grünberg, G. Güntherodt, A. Frey, W. Kress, H. Bilz, M. Cardona, K. Fischer, and W. Zinn (unpublished).
- <sup>35</sup>J. Vitins and P. Wachter, *AIP Conference Proceedings of the 21st Annual Conference on Magnetism and Magnetic Materials*, (AIP, New York, 1975), p. 662.
- <sup>36</sup>J. Vitins and P. Wachter, *Solid State Commun.* **17**, 911 (1975).
- <sup>37</sup>J. Vitins and P. Wachter, *J. Magn. Magn. Mater.* **3**, 161 (1976).
- <sup>38</sup>J. Vitins and P. Wachter, *International Conference on Magnetism, Amsterdam, 1976* (unpublished).
- <sup>39</sup>L. E. Schmutz, V. J. Tekippe, M. S. Dresselhaus, and R. L. Aggarwal (unpublished).
- <sup>40</sup>S. A. Safran, G. Dresselhaus, M. S. Dresselhaus, and B. Lax, *Physica (Utr.)* **89 B**, 229 (1977).
- <sup>41</sup>S. A. Safran, B. Lax, and G. Dresselhaus, *Solid State Commun.* **19**, 1217 (1976); **20**, vii(E) (1976).
- <sup>42</sup>E. Anastassakis and E. Burstein, *J. Phys. C* **5**, 2468 (1972).
- <sup>43</sup>J. D. Axe, *J. Phys. Chem. Solids* **30**, 1403 (1969).
- <sup>44</sup>M. Ikezawa and T. Suzuki, *J. Phys. Soc. Jpn.* **35**, 1556 (1973).
- <sup>45</sup>L. Passell, O. W. Dietrich, and J. Als-Nielsen, *Phys. Rev. B* **14**, 4897 (1976); J. Als-Nielsen, O. W. Dietrich, and L. Passell, *ibid.* **14**, 4908 (1976); O. W. Dietrich, J. Als-Nielsen, and L. Passell, *ibid.* **14**, 4923 (1976).
- <sup>46</sup>P. Wachter, *Phys. Kondens. Mater.* **8**, 80 (1968).
- <sup>47</sup>J. A. Osborne, *Phys. Rev.* **67**, 351 (1945).
- <sup>48</sup>R. I. Joseph and E. Schlömann, *J. Appl. Phys.* **36**, 1579 (1965); further demagnetization corrections accounting for the shape of the laser-heated scattering volume proved negligibly small.
- <sup>49</sup>P. L. Kapitza, *J. Phys. USSR* **4**, 181 (1941).
- <sup>50</sup>T. H. K. Frederking, *Chem. Eng. Prog. Symp. Ser.*, J. A. I. Ch. E. **64**, 21 (1968); B. W. Clement and T. H. K. Frederking, *Bull. Intern. Inst. Refrig. Annexe* **49** (1966-5).
- <sup>51</sup>P. Wachter, *Phys. Kondens. Mater.* **7**, 1 (1968). Due to optical activity, birefringence or Faraday rotation, the AF-I and ferrimagnetic domains also depolarize the light which passes through the bulk of the crystal. Polarization selection rules are therefore difficult to observe in the right-angle configuration, although they can be studied in the back-scattering geometry ( $E_L > E_R$ ), where the skin depth, and thus the depolarization effects, are very small.
- <sup>52</sup>T. B. Reed and R. H. Fahey, *J. Cryst. Growth* **8**, 337 (1971).
- <sup>53</sup>G. E. Everett (private communication).
- <sup>54</sup>J. Schoenes and P. Wachter, *Physica B* **89**, 155 (1977).
- <sup>55</sup>G. Busch, *J. Appl. Phys.* **38**, 1386 (1967).
- <sup>56</sup>G. Busch, J. Schoenes, and P. Wachter, *Solid State Commun.* **8**, 1841 (1970).
- <sup>57</sup>The data have been corrected for instrumental response, laser heating effects, and the  $\omega^4$  dependence of the Raman cross section.
- <sup>58</sup>The spectrometer grating efficiency has a polarization dependence which is a function of the incident wavelength and must be taken into account.
- <sup>59</sup>W. Zinn, *J. Magn. Magn. Mater.* **3**, 23 (1976).
- <sup>60</sup>J. L. Birman, *Phys. Rev. B* **9**, 4518 (1974).
- <sup>61</sup>J. Schoenes, P. Wachter, and F. Rys, *Solid State Commun.* **15**, 1891 (1974).
- <sup>62</sup>M. J. Freiser, *IEEE Trans. Magn. MAG-4*, 152 (1968).
- <sup>63</sup>S. A. Safran, G. Dresselhaus, and B. Lax, *Phys. Rev. B* **16**, 2749 (1977) (following paper).

<sup>64</sup>Y. Ousaka, O. Sakai, and M. Tachiki (unpublished).

<sup>65</sup>Calculated from the data presented in Y. Shapira and T. B. Reed, *Proceedings of the Conference on Magnetism and Magnetic Materials, 1974* (American Institute of Physics, New York, 1974), p. 837.

<sup>66</sup>R. K. Ray, J. C. Tsang, R. L. Aggarwal, M. S. Dresselhaus, and T. B. Reed, *Phys. Lett. A* **37**, 129 (1971).

<sup>67</sup>J. C. Tsang, M. S. Dresselhaus, R. L. Aggarwal, and T. B. Reed, *Proceedings of the Eleventh International Conference on the Physics of Semiconductors, Warsaw,*

*Poland, 1972* (PWN-Polish Scientific, Warsaw, 1972), p. 1273.

<sup>68</sup>R. P. Silberstein, M. S. Dresselhaus, and G. Dresselhaus, *Bull. Am. Phys. Soc.* **22**, 340 (1977).

<sup>69</sup>G. D. Holah, J. S. Webb, R. B. Dennis, and C. R. Pidgeon, *Solid State Commun.* **13**, 209 (1973); C. R. Pidgeon, G. D. Holah, R. B. Dennis and J. S. Webb, in Ref. 67, p. 1280.

<sup>70</sup>R. P. Silberstein, V. J. Tekippe, and M. S. Dresselhaus (unpublished).